A Critical Analysis of Turbulence Dissipation in Near Wall flows, based on Stereo Particle Image Velocimetry and Direct Numerical Simulation data

William George, Michel Stanislas, Jean Marc Foucaut, Christophe Cuvier, Jean Philippe Laval

A Critical Analysis of Turbulence Dissipation in Near Wall flows, based on Stereo Particle Image Velocimetry and Direct Numerical Simulation data

William K. George[1] Michel Stanislas[2] Jean Marc Foucaut[3]
Christophe Cuvier[3] Jean Philippe Laval[3]

September 18, 2022

[1] Visiting Pr., Centrale Lille, F59651 Villeneuve d'Ascq, France
[2] Pr. Emeritus, Centrale Lille, F59651 Villeneuve d'Ascq, France
[3] Univ. Lille, CNRS, ONERA, Arts et Metiers Institute of Technology, Centrale Lille, UMR 9014 - LMFL - Laboratoire de Mécanique des Fluides de Lille - Kampé de Fériet, F-59000 Lille, France

Abstract

An experiment was performed using Stereo Particle Image Velocimetry (SPIV) in the Laboratoire de Mécanique des Fluides de Lille boundary layer facility to determine all the derivative moments needed to estimate the average dissipation rate of the turbulence kinetic energy $\epsilon = 2\nu\langle s_{ij}s_{ij}\rangle$ where s_{ij} is the fluctuating strain-rate and $\langle\ \rangle$ denotes ensemble averages. Also measured were all the moments of the full average deformation rate tensor, as well as all of the first, second and third fluctuating velocity moments except those involving pressure. The Reynolds number was $Re_\theta = 7634$ or $Re_\tau = 2598$.

The present paper gives the measured average dissipation, ϵ and the derivative moments comprising it. The results are compared to the earlier measurements of [Balint et al., 1991, Honkan and Andreopoulos, 1997] at lower Reynolds numbers and to new results from a plane channel flow DNS at comparable Reynolds number. Of special interest is the prediction by [George and Castillo, 1997, Wosnik et al., 2000] that $\epsilon^+ \propto {x_2^+}^{-1}$ for streamwise homogeneous flows and a nearly indistinguishable power law, $\epsilon \propto {x_2^+}^{\gamma-1}$, for boundary layers. In spite of the modest Reynolds number, the predictions seem to be correct.

Then the statistical character of the velocity derivatives is examined in detail, and a particular problem is identified with the breakdown of local homogeneity inside $x_2^+ = 100$. A more general alternative for partially homogeneous turbulence flows is offered which is consistent with the observations. With the help of DNS, the spatial characteristics of the dissipation very near the wall are also examined in detail.

1 Introduction

One of the most important parameters of modern turbulence theories and attempts to model turbulence is the average rate at which energy per unit mass, say ϵ, is dissipated through turbulence. It not only

describes the actual dissipation of kinetic energy by deformation of the fluid elements [Batchelor, 1967], it is also important to discussions of interscale energy transfer because of its relation to the spectral flux of energy from large to small scales [Tennekes and Lumley, 1972, George, 2014]. Unfortunately the actual dissipation rate is also one of the most elusive quantities to obtain experimentally, mainly because of the small scale motions (typically fractions of a *mm* in laboratory flows) and small spectral amplitudes which must be resolved to measure it correctly.

This paper tries to extends the state-of-the art by combining measurements in a moderately high Reynolds number turbulent boundary layer ($R_\theta = 7634$ with $R_\theta = \theta U_e/\nu$ where U_e is the external velocity, θ is the momentum thickness and ν the kinematic viscosity) using Dual Plane Stereo Particle Image Velocimetry (DP-SPIV) and highly resolved Direct Numerical Simulation (DNS) in a channel at comparable Reynolds number. The DNS is described in detail in section 3. The experiment takes advantage of the unique boundary layer (BL) facility at Laboratoire de Mécanique des Fluides de Lille (LMFL, former LML) which can achieve boundary layers of up to 30 cm in thickness at Reynolds numbers up to $R_\theta = 20,000$ at speeds up to 10 m/s. The large length scales and low mean velocities allow state-of-the-art SPIV to resolve scales small enough to obtain reasonable estimations of the dissipation, while still insuring that the scattering particles follow the flow. But what really makes this experiment possible are two "tricks" used to reduce the SPIV quantization noise which would otherwise have prevented accurate derivative measurement.

PIV typically has resolutions of less than 1:100 relative to the mean velocity, and this "PIV noise" is of order one (even much larger) when velocity differences at the scale of the Kolmogorov microscale are computed. When this noise is squared, it overwhelms the derivative. In the present contribution, by using crossed-planes SPIV, the noise contribution to the 'measured' derivative moments could be removed. A second "trick" was to use the continuity equation multiplied by one derivative and averaged so that all squared moments could be computed independently from only cross-moments. This could be used at all measurement locations. The experiment and the noise reduction techniques used are described briefly below, and in detail in [Foucaut et al., 2021].

In the present contribution, after briefly describing the DNS and experiment used, the dissipation data obtained are presented and validated against DNS and previous experimental data. A particular emphasis is put on the behaviour of dissipation in the mesolayer. In a second step, the different classical hypotheses — *local isotropy*, *local axisymmetry* and *local homogeneity* — are examined in detail for the whole flow before focussing on the very near wall region below $x_2^+ = 100$ (x_1 being the streamwise, x_2 the wall-normal and x_3 the spanwise coordinates, $x_2^+ = x_2.u_\tau/\nu$ with u_τ the wall friction velocity). Finally the available DNS data is used to look at the spatial structure near the wall of the main components of the dissipation tensor, before drawing some conclusions.

2 What is the dissipation?

Before entering into the details of this contribution, it is important to clearly define the parameters of interest.

2.1 The definition of dissipation

The instantaneous rate of dissipation of kinetic energy, $\tilde{\epsilon}$ (or simply *dissipation*) in any flow of any Newtonian fluid is defined to be:

$$\tilde{\epsilon} = 2\nu \left[\tilde{s}_{ij}\tilde{s}_{ij} - \frac{1}{3}\tilde{s}_{kk}\tilde{s}_{kk} \right] \tag{1}$$

The tilde is used to represent an instantaneous quantity, ν is the kinematic viscosity, $\tilde{s}_{ij}$ is the instantaneous strain-rate defined by:

$$\tilde{s}_{ij} = \frac{1}{2}\left[\frac{\partial \tilde{u}_i}{\partial x_j} + \frac{\partial \tilde{u}_j}{\partial x_i} \right] \tag{2}$$

where $\tilde{u}_i$ is the instantaneous velocity fluctuation. For an incompressible fluid flow like that considered herein, $\tilde{s}_{kk} = 0$, so the last term of equation (1) will be dropped in the remainder of this paper. The reason this is the true dissipation is NOT that the terms are all positive – in fact 3 of them are usually negative. But it is this full $\tilde{\epsilon}$ that shows up with negative sign in the entropy equation. So it always acts to reduce the kinetic energy locally, and send it irreversibly to internal energy.

2.2 The average dissipation rate.

In turbulence studies, since the instantaneous flow is usually out of reach in practical conditions, it is the Reynolds averaged equations or spectral equations which are solved. So it is the average dissipation rate,

$$\epsilon \equiv \langle \tilde{\epsilon} \rangle = \langle 2\nu \tilde{s}_{ij}\tilde{s}_{ij} \rangle \tag{3}$$

that is of primary interest. **Hereafter in this paper the symbol, ϵ, will refer to the averaged dissipation rate, or simply "the dissipation".**

It is frequent in DNS, but also recently in reported experiments as well, to report on the averaged values of the '*pseudo-dissipation*', which is classicaly used in turbulence models of the Turbulence Kinetic Energy (TKE) equation:

$$\mathcal{D} \equiv \nu \langle \left[\frac{\partial u_i}{\partial x_j} \right]^2 \rangle, \tag{4}$$

First note that $\tilde{\mathcal{D}} = \nu(\partial \tilde{u}_i/\partial x_j)^2$ is not the instantaneous dissipation. The reason is of course that it contains both strain-rate and rotation-rate contributions, and the latter do not dissipate energy [Batchelor, 1967]. But when averaged quantities are considered, the difference between ϵ and $\mathcal{D}$ is often slight. This is due to the fact that high Reynolds number turbulence is often nearly *locally homogeneous* [George and Hussein, 1991]. In homogeneous flows $\langle s_{ij}s_{ij} \rangle = \langle \frac{1}{2}\omega_i\omega_i \rangle = \langle \omega_{ij}\omega_{ij} \rangle$, where ω_i is the vorticity and ω_{ij} is the rotation-rate tensor [Tennekes and Lumley, 1972, George and Hussein, 1991].

If, instead of the Turbulence Kinetic Energy (TKE) equation, the full Reynolds stress transport system is looked at, then the dissipation takes the shape of a tensor:

$$\epsilon_{ij} = 2\nu \langle \frac{\partial u_i}{\partial x_l}\frac{\partial u_j}{\partial x_l} \rangle + \nu \langle \frac{\partial u_l}{\partial x_i}\frac{\partial u_j}{\partial x_l} \rangle + \nu \langle \frac{\partial u_l}{\partial x_j}\frac{\partial u_i}{\partial x_l} \rangle \tag{5}$$

and the '*pseudo-dissipation*' is also a tensor:

$$\mathcal{D}_{ij} = 2\nu \langle \frac{\partial u_i}{\partial x_l}\frac{\partial u_j}{\partial x_l} \rangle \tag{6}$$

2.3 Measuring the true dissipation

To obtain the average dissipation rate, $\epsilon = 2\nu\langle s_{ij}s_{ij}\rangle$ experimentally it is necessary to measure all its components. This in turn requires measuring the variance of each velocity derivative term together with a few covariances of them. There are a total of twelve terms which can be organized into three groups [George and Hussein, 1991]:

$$\begin{aligned}\epsilon \quad = \nu \Bigg\{ & 2\left[\left\langle\left[\frac{\partial u_1}{\partial x_1}\right]^2\right\rangle + \left\langle\left[\frac{\partial u_2}{\partial x_2}\right]^2\right\rangle + \left\langle\left[\frac{\partial u_3}{\partial x_3}\right]^2\right\rangle\right] \\ & + \left[\left\langle\left[\frac{\partial u_1}{\partial x_2}\right]^2\right\rangle + \left\langle\left[\frac{\partial u_2}{\partial x_1}\right]^2\right\rangle + \left\langle\left[\frac{\partial u_1}{\partial x_3}\right]^2\right\rangle\right. \\ & \qquad \left. + \left\langle\left[\frac{\partial u_3}{\partial x_1}\right]^2\right\rangle + \left\langle\left[\frac{\partial u_2}{\partial x_3}\right]^2\right\rangle + \left\langle\left[\frac{\partial u_3}{\partial x_2}\right]^2\right\rangle\right] \\ & + 2\left[\left\langle\frac{\partial u_1}{\partial x_2}\frac{\partial u_2}{\partial x_1}\right\rangle + \left\langle\frac{\partial u_1}{\partial x_3}\frac{\partial u_3}{\partial x_1}\right\rangle + \left\langle\frac{\partial u_2}{\partial x_3}\frac{\partial u_3}{\partial x_2}\right\rangle\right]\Bigg\} \end{aligned} \tag{7}$$

Note that the first nine are squared, but only the diagonals (top line) and crossed-moments (bottom line) have a factor of 2 in front of them. The last line involves only cross-moments which are usually negative. Obviously any attempt to determine the dissipation by experiment is especially difficult because of the large number of velocity derivatives which must be measured and the difficulty of measuring them in real turbulent flows. As a result, all measurements to-date have had to make assumptions about the turbulence which are not necessarily valid.

For the measurements preceding ours reported here (all with hot-wires and in Turbulent Boundary Layers (TBL)) it was difficult to measure accurately because of the high spatial resolution required [Wyngaard, 1968, George and Taulbee, 1992, Ewing et al., 1995, Ewing and George, 2000]. Only in the past few decades has it been possible to measure more than as few derivatives at a time, and even this required extraordinary efforts (c.f. [Balint et al., 1991, Honkan and Andreopoulos, 1997, Tsinober et al., 1992, Andreopoulos and Honkan, 2001, Gulitski et al., 2007]). All used Taylor's frozen field hypothesis for the streamwise derivatives. More recent attempts have been made using PIV, but most of these also used Taylor's hypothesis in some form.

For some recent PIV measurements (e. g. , [Carlier and Stanislas, 2005, Herpin et al., 2012]), spatial resolution has been less of a problem than with hot-wires; but as noted above the limited dynamical range (typically less than 1:100) and the resulting noise present serious problems, since many of the derivatives needed are squared. Time-resolved PIV has not contributed significantly for two reasons. First of all, the data rates are simply not high enough yet to obtain a reasonable time derivative in air at the scales needed. But second and more fundamentally, Taylor's frozen field hypothesis has always been a serious issue when using time-derivatives (c.f. [Antonia et al., 1980, George et al., 1989, Lumley, 1995]). The fundamental problem is that the convection velocity is fluctuating and this "leaks" energy down the derivative spectrum, so serious over-estimates of the derivative moments are common [Champagne, 1978]. Even more serious problems with many measurements to-date arise from the need to make assumptions about the statistics (e.g., isotropy, homogeneity, etc.) to fill in the missing terms.

2.4 The goal of this paper

This paper will present our data and compare it to previous attempts to measure the dissipation and velocity derivatives in turbulent boundary layers. Of particular interest will be the data of [Balint et al., 1991] and [Honkan and Andreopoulos, 1997, Andreopoulos and Honkan, 2001] who published experimental results of the dissipation rate obtained in a turbulent boundary layer with specially designed multiwires probes (Note that the experiments of [Tsinober et al., 1992] were of great interest as well, but we simply could not make their data fit our plots with the scaling parameters provided). All of the DNS results for turbulent boundary layers (at least until very recently) are of much lower Reynolds number than the present experiment and therefore are of limited interest. Only [Antonia et al., 1991] examined the different hypotheses using DNS results from a channel flow at low Reynolds number. Unfortunately many of the more recent DNS results which are at Reynolds numbers comparable to the present data did not catalog all of the necessary derivative moments to compute the true dissipation. For this reason, a specific channel flow DNS performed by [Thais et al., 2011] was used for comparison here as all the necessary data were provided by the authors. The characteristics of this DNS are summarized in section 3. It was expected to not be too different from a boundary layer in the near wall and log regions, nor was it.

This contribution presents the first measurements of all derivatives in a turbulent turbulent boundary layer at moderate Reynolds number using Dual-Plane-Stereoscopic PIV (or DP-SPIV). SPIV is applied in two normal planes to compute all the derivatives of the three velocity components. Both the true dissipation rate, ϵ, and the pseudo-dissipation rate, $\mathcal{D}$, are evaluated. It also uses these new results and those of the channel flow DNS at comparable Reynolds number to evaluate previous measurements and theoretical predictions.

Then the assumptions usually made about the velocity derivatives and the dissipation (and enstrophy) inferred from them are examined in detail. Of particular interest is whether the velocity derivative moments in turbulent boundary layers can be assumed to be *locally isotropic*, *locally axisymmetric*, or even *locally homogeneous*. Also considered are the tensors, ϵ_{ij} and $\mathcal{D}_{ij}$ which appear in the Reynolds stress balance equations. Finally, the spatial distribution of the building terms of the turbulence dissipation is examined near the wall.

3 Description of the channel flow DNS computation

At the time of this work, there were no easily accessible DNS data sets which included the velocity derivative cross-velocity moment data. (For example, even the recent relatively high Reynolds number data [Hoyas and Jiménez, 2008] is missing these moments.) Fortunately our colleagues (L. Thais and co-workers) made their $Re_\tau = 3000$ data available to us for post-processing. So the DNS results used in the present work were obtained by L. Thais and co-workers using a massively parallel code described in [Thais et al., 2011] for the direct numerical simulation of Newtonian or viscoelastic turbulent channel flow. The spatial discretization uses Fourier modes in the two periodic streamwise and spanwise directions and 6^{th}-order compact finite differences in the normal direction. The Reynolds number based on friction velocity and half channel height is $Re_\tau = 3000$. The discretized equations were integrated on a domain of size $8\pi \times 2 \times 3\pi/2$ with a spatial resolution $5120 \times 768 \times 2048$ in streamwise (x_1), normal (x_2) and spanwise (x_3) directions respectively. The first grid point in the normal direction is located at $\Delta^+_{x_2} = 0.5$ from each wall and up to 18 points are used to discretize the first 10 wall units. The spatial discretizations in the streamwise and spanwise directions are $\Delta^+_{x_1} = 11$ and $\Delta^+_{x_3} = 7$ respectively. The simulation was performed on IBM Blue Gene/Q computer running at the IDRIS/CNRS computing center, Orsay, France.

Up to 40 velocity fields were recorded but only the last 7 were used to compute the dissipation terms of the present analysis. These fields are separated by a non-dimensional time of 1.5 based on the bulk velocity and the half channel height. This corresponds to $\Delta t^+ = 200$ in wall unit time. The dissipation terms were computed in physical space on the full domain using an 8^{th}-order compact finite difference scheme for the derivatives in order to maintain accuracy.

Figure 1 shows a comparison of the Reynolds normal stresses of the present DNS with the DNS of [Hoyas and Jiménez, 2006] at $Re_\tau = 2000$ and the recent DNS of [Lee and Moser, 2015] at $Re_\tau = 5200$. The three simulations agree very well in the near wall region. The first peak of u_1' which weakly depends on the Reynolds number lies within the two other DNS. The Reynolds number effect is clearly visible in the outer part, with the beginning of a plateau at the highest Reynolds number.

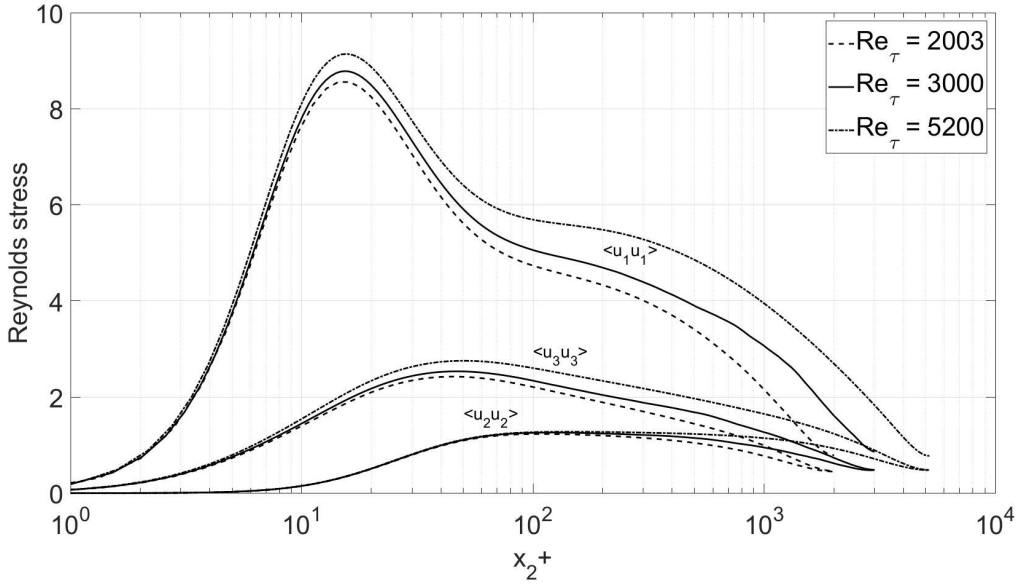

Figure 1: Comparison of the Reynolds stresses of the DNS of [Thais et al., 2011] at $Re_\tau = 3000$ with the DNS of [Hoyas and Jiménez, 2006] at $Re_\tau = 2003$, the DNS of [Lee and Moser, 2015] at $Re_\tau = 5200$.

Figure 2 shows the homogeneous dissipation $\mathcal{D}$ in inner variables along with that computed by [Hoyas and Jiménez, 2006] and [Lee and Moser, 2015] for a plane channel and the data of [Sillero et al., 2013] for a Zero Pressure Gradient (ZPG) turbulent boundary layer. Here, $\mathcal{D}$ was chosen instead of ϵ in order to compare the different data sets as not all of them provided the full dissipation. Also, the dissipation $\mathcal{D}^+$ has been premultiplied by the wall distance x_2^+. The reason for this representation will be justified in detail in the following; but it can already be noted that it emphasises the Reynolds number influence in the outer part for the channel flow, the overlap region, and the difference between the channel and the boundary layer in the same outerpart.

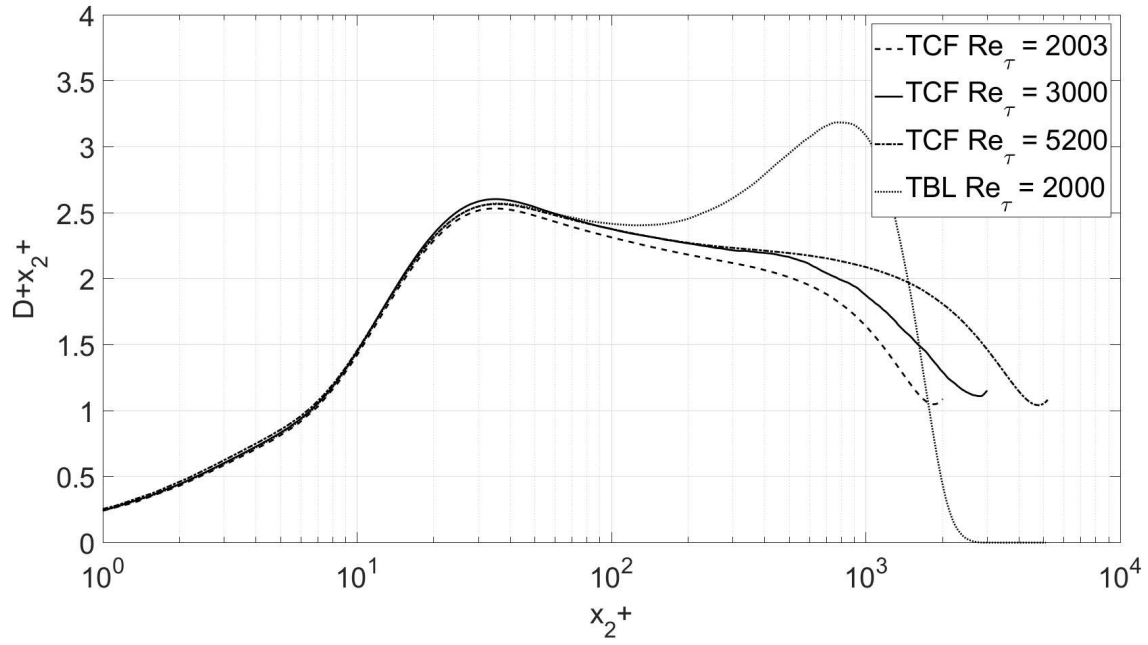

Figure 2: Comparison of the premultiplied pseudo-dissipation $\mathcal{D}x_2$ (Eq.(4)) of the channel flow DNS of [Thais et al., 2011] at $Re_\tau = 3000$ with the DNS of [Hoyas and Jiménez, 2006] at $Re_\tau = 2003$, the DNS of [Lee and Moser, 2015] at $Re_\tau = 5200$. and the boundary layer DNS of [Sillero et al., 2013]

4 The experiment

The experiment was carried out in the Lille turbulent boundary layer wind tunnel. The optically accessible test section has been extended to the full tunnel length, and is 1 m high, 2 m wide and 20 m long. The long length allows the development of the boundary layer so that its thickness is close to 30 cm at 20 m. The external flow has a slightly positive pressure gradient. The tunnel and flow quality has been documented in many previous papers [Carlier and Stanislas, 2005, Stanislas et al., 2008, Herpin et al., 2012].

Stereoscopic PIV (or SPIV) is now a recognized method for measuring turbulent flows. Many researchers have previously used this method to compute statistics of the flow such as mean velocity, Reynolds stress tensor, probability density functions and even spectra ([Adrian et al., 2000, Foucaut et al., 2011, Herpin et al., 2012]). A detailed discussion of the measurement technique and especially the validation of it is available in [Foucaut et al., 2021]. Therefore we present only the briefest detail below.

4.1 The dual plane SPIV setup

SPIV allows the measurement of the three components of the velocity in a plane with an accuracy of about 1-2% (0.1 pixel), but the limited spatial resolution (typically millimeters) cannot easily resolve the

smallest scales of the flow. To compute the dissipation components, both differentiation and statistical computations are involved; and additional difficulties arise from the noise amplification when derivatives have to be computed from discrete realizations [Foucaut and Stanislas, 2002].

The capabilities of the SPIV technique can be increased by the use of the light polarization to record velocity fields in two different planes simultaneously. When the planes are parallel, this method is called dual plane stereoscopic PIV [Kahler and Stanislas, 2000]. The dual plane technique allows the measurement of two velocity fields with an adjustable time delay or spatial separation between them. By varying this delay, the space-time correlation of the velocity field can be computed. And by varying the separation, the 3D spatial correlation can be obtained. [Ganapathisubramani et al., 2005a] used the dual plane technique to get the full gradient tensor and to study the near wall flow structures.

In the present experiment, the field of view was imaged with two Stereoscopic PIV systems in two normal planes, both orthogonal to the wall. The flow was seeded using Poly-Ethylene Glycol particles in the return circuit of the tunnel just after the fan. The particle size was of the order of 1 μm and the particle image size of the order of 1.8 pixel on the cameras. Following [Raffel et al., 1998], such a size should lead to weak peak-locking, but none was apparent in the velocity probability density functions's (pdf) shown in [Foucaut et al., 2021].

Figure 3 gives an example of instantaneous streamwise velocity field recorded with the present set-up. The images from both cameras were processed with a standard multi-grid and multi-pass algorithm with image deformation [Scarano, 2002]. The final interrogation window size was 24 x 32 pixels for each plane. Such a size corresponds to a square window in the physical space of 1.4 x 1.4 mm^2 (11.6 x 11.6 wall units). A mean overlap of about 66% was used. The light sheet thickness varied from about 0.6 mm closest to the wall to 2 mm at the outermost location. [Foucaut et al., 2021] present a detailed analysis of the spatial resolution effects on the measurements.

4.2 Data processing and noise removal

The primary problem with using PIV for derivative measurement is the PIV noise. For example, the derivative 'signal' after processing, say $s(t)$, can be presented as $s(t) = d(t) + n(t)$ where $d(t)$ is the true derivative as a function of time, and $n(t)$ is the 'noise' (or difference) between the true and measured signal. $n(t)$ can be thought of as a square-wave of random amplitude (see [Wänström et al., 2007]). So squaring and averaging yields $\langle s^2 \rangle = \langle d^2 \rangle + \langle n^2 \rangle$. Note that we have assumed the noise to be uncorrelated with the signal. For derivative measurement using SPIV, $\langle n^2 \rangle$ can be greater than $\langle d^2 \rangle$, even sometimes much greater.

If, however, both planes are perpendicular and cross each other, additional information about the spatial properties of the flow can be obtained [Hambleton et al., 2006, Ganapathisubramani et al., 2005b]. But more importantly for the present experiment, it provides a unique opportunity to evaluate noise-free derivative moment by choosing each term in the derivative product from different planes (since the noise is uncorrelated between the two planes). For example, if $s_1(t)$ and $s_2(t)$ measure the same velocity but from different planes, then their cross-correlation is given by:

$$\langle s_1(t) s_2(t) \rangle = \langle d_1(t) d_2(t) \rangle + \langle n_1(t) n_2(t) \rangle \tag{8}$$

But $\langle d_1(t) d_2(t) \rangle = \langle d(t)^2 \rangle$ if they measure the same (or nearly the same) interrogation volume. And since the noise sources are statistically independent (or at least uncorrelated), $\langle n_1(t) n_2(t) \rangle = 0$. This eliminates a primary source of noise in the estimation of the dissipation since almost all the derivative moments are squared quantities.

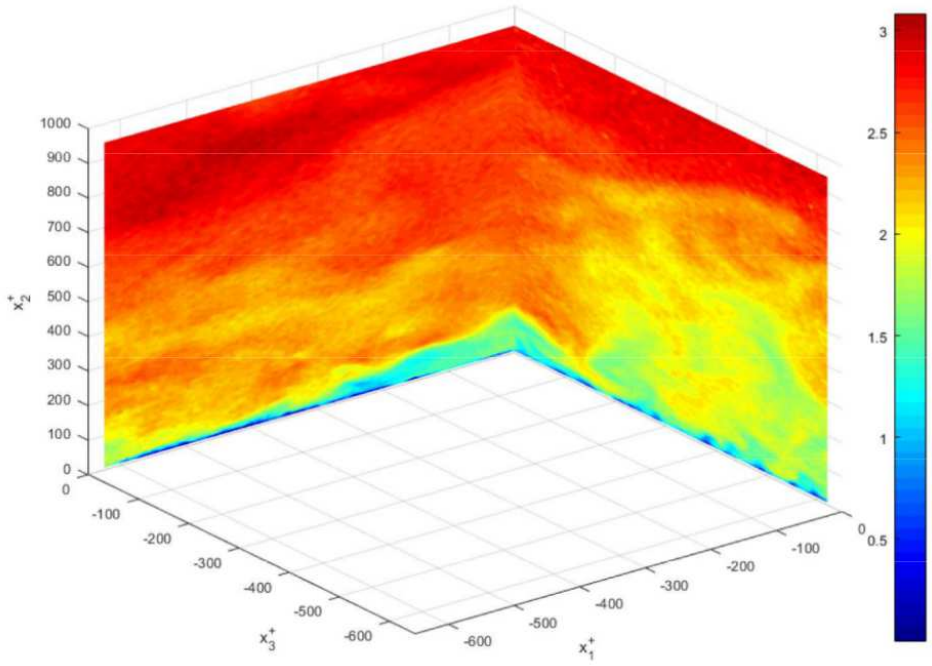

Figure 3: Example of an instantaneous streamwise velocity field using cross-plane SPIV.

The other "trick" used here was to employ the continuity equation multiplied by one of the derivatives of interest, i.e.,

$$\frac{\partial u_m}{\partial x_n}\left[\frac{\partial u_1}{\partial x_1}+\frac{\partial u_2}{\partial x_2}+\frac{\partial u_3}{\partial x_3}\right]=0 \tag{9}$$

Setting $m, n = 1$ for example yields:

$$\left[\frac{\partial u_1}{\partial x_1}\right]^2=-\left[\frac{\partial u_1}{\partial x_1}\frac{\partial u_2}{\partial x_2}+\frac{\partial u_1}{\partial x_1}\frac{\partial u_3}{\partial x_3}\right] \tag{10}$$

So all of the diagonal terms in the dissipation tensor can be computed from 'noise-free' cross-moments. Finally derivatives were also computed using the 'de-noising' methodology of [Foucaut and Stanislas, 2002].

4.3 Temporal and spatial resolution

Figure 4 shows that the time-scale ratio for the scattering particles (sometimes referred to as Stokes number, St^+) is much less than one. So indeed the particles contributing to the velocity in the interrogation volume can be assumed to follow the flow at the dissipative scales.

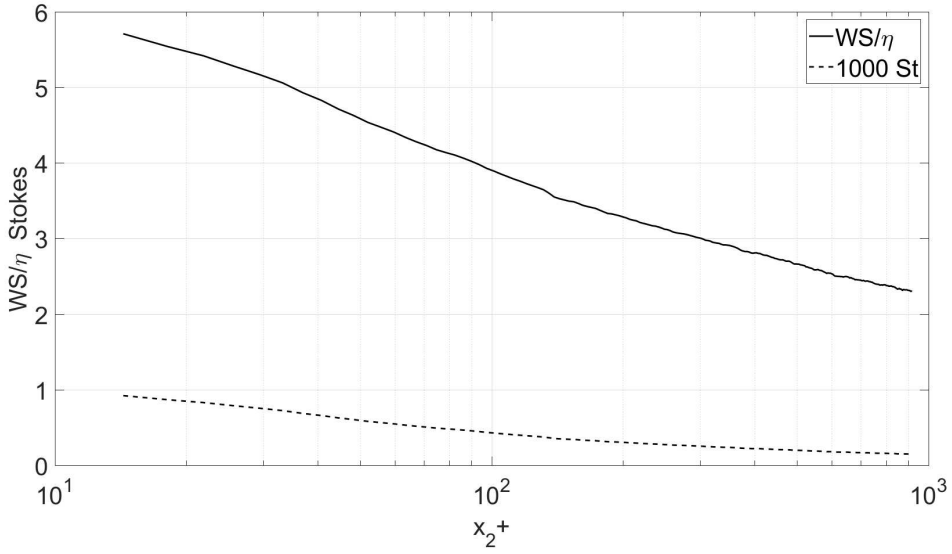

Figure 4: Interrogation window size WS normalized by the Kolmogorov microscale, $(\nu/\epsilon)^{1/4}$ and particle time scale normalized by the Kolmogorov microtime scale, $(\nu/\epsilon)^{1/2}$. Wall distance x_2 normalized by ν/u_τ using the data in *table* 1

.

Also shown in figure 4 is the ratio of largest dimension of the SPIV interrogation window size, say WS, to the Kolmogorov microscale, $\eta = (\nu^3/\epsilon)^{1/4}$, estimated from the data. The values range from 2 at the outermost points of our measurement to 6 at the innermost. These are almost identical to those reported by [Balint et al., 1991, Honkan and Andreopoulos, 1997], suggesting any differences cannot be attributed to the size of the averaging volume. Here, thanks to the overlap of 66% of the interrogation windows (which gives a grid point in the data every 4η at worst, with 33% of new information in the interrogation window), one can expect an effective spatial resolution slightly better than the interrogation window size WS that is varying between 5η and η from the wall outward.

Since about 99% of the dissipation lies at spectral wavenumbers k below $k\eta = 1$, it requires $WS \leq \pi\eta$ [George and Taulbee, 1992] to resolve the entire derivative spectrum. But since ϵ is an integral under the dissipation spectrum which has a long exponential tail, somewhat larger ratios are indicated to be acceptable [Wyngaard, 1968, Ewing et al., 1995, Ewing and George, 2000]. So for most of our flow spatial filtering should not be an issue, except perhaps at the closest wall positions. The whole subject of spatial filtering is of considerable interest, and is addressed in detail in [Foucaut et al., 2021].

Table 1: Experimental flow parameters: U_e external velocity, δ boundary layer thickness, $\delta*$ displacement thickness, θ momentum thickness, u_τ wall friction velocity, $R_{e\theta}$ momentum Reynolds number, $R_{e\tau}$ friction Reynolds number, C_f friction coefficient.

Ue	δ	$\delta*$	θ	u_τ	Re_θ	Re_τ	C_f
3 m/s	0.32 m	48.2 mm	36.2 mm	0.113 m/s	7634	2598	0.00275

5 Experimental Results

This section presents the measured derivative moments and compares them to earlier measurements and DNS. For the purpose of conciseness, only some representative samples are presented here. The whole set of data and plots are made available as complementary electronic material to the paper.

5.1 Experimental parameters and velocity moments

The present experiment was carried out at a Reynolds number R_θ of 7634 (δ^+ of 2598) which corresponds to a free stream velocity of 3 m/s. Table 1 summarizes the important boundary and integral parameters for this experiment.

Figure 5 shows the mean streamwise velocity measured from the two PIV planes and compares it with hot wire anemometry (HWA) data. Figure 6 gives the turbulence intensity profiles measured from the same two PIV planes, also compared with hot wire anemometry (HWA) and DNS data. These results are in very good agreement above 15 wall units, except for the spanwise turbulence intensity component $\sqrt{\langle u_3^2 \rangle}$ from the hot wire in figure 6. These data obviously depart from the PIV and the DNS below 40 wall units. This can be attributed to hot-wire errors resulting from the mean velocity gradient at the scale of the X-wire probe and cross-flow errors from the increasing local turbulence intensity near the wall, neither of which can be taken into account by calibration. For the same component, the data from the x_1x_2 plane are a bit lower very near the wall than the x_2x_3 and DNS ones as the u_3 component is out of plane in the x_1x_2 plane. As far as $\sqrt{\langle u_1^2 \rangle}$ is concerned, the peak level is slightly underestimated by both PIV planes and the x_1x_2 measurements seem more sensitive to the limited spatial resolution. Finally, also close to the wall, $\sqrt{\langle u_2^2 \rangle}$ is in good agreement between the PIV and hot wire data (especially in the x_1x_2 plane), but departing from the DNS when approaching the wall. This can be attributed to a lack of spatial resolution in both cases, agravated by the fact that this is the smallest component of the three. Beside these very near wall problems, the agreement is quite good between the two PIV planes, the HWA and the DNS.

5.2 Measured derivative moments

The derivatives were computed by the methods described briefly in Section 4.2, and in detail in [Foucaut et al., 2021]. Based on the accuracy analysis performed in [Foucaut et al., 2021], the data are supposed to be valid to within a few percent for $x_2^+ > 25$, indicated by the vertical dashed line on the plots. But as will be seen, this analysis does not take into account the spatial filtering. The term $\langle (\partial u_3/\partial x_1)(\partial u_1/\partial x_3) \rangle$ was computed only at the intersection of the two SPIV planes and cannot therefore be averaged along one of the two planes, so it shows more scatter than the other profiles. Table 2 summarizes how each

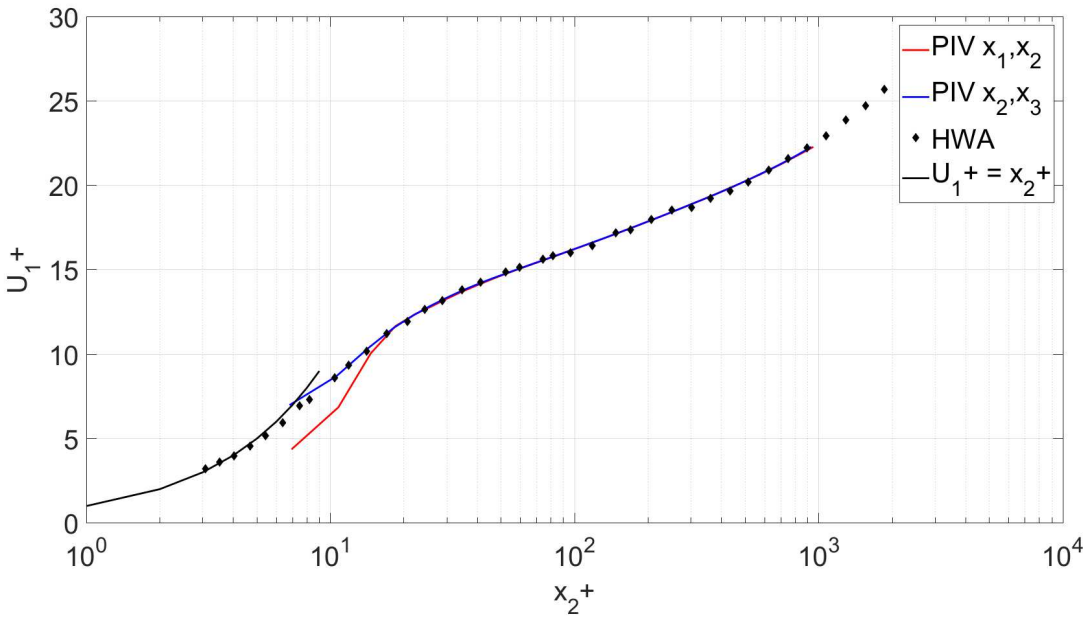

Figure 5: Mean velocity profiles of the two PIV planes compared to hot-wire data of [Carlier and Stanislas, 2005] (With permission of *Exp. in Fluids*).

derivative moment was obtained and which corrections were applied. Details on the corrections are given in Foucaut et al. [2021].

Figure 7 shows profiles of all twelve derivative moments contributing to the true dissipation ϵ (Eq. [7]) as linear-log plots premultiplied by x_2^+. It is clear that the derivative moments are not all the same. Ratios of 10 or even more are observed near $x_2^+ = 20$. This has an interesting experimental consequence: it is probably not necessary to measure all the components of ϵ to have a good estimation of it. In particular, it should be noted that all cross products are negative. The questions of whether the derivative moments are *locally homogenous*, *locally axisymmetric* or *locally isotropic* will be addressed in detail in Sections 6 to 8, together with the question of their individual contribution to the total dissipation. Note that even though many moments peak strongly near the wall, some go to zero at $x_2 = 0$. Note also that none of our measurements go to zero at large values of x_2 since measurements were not taken outside of the overlap (or log) region.

In figure 7 all the derivative moments have been multiplied on purpose by x_2. This puts clearly in evidence what will be a key result of the present contribution: the fact that the dissipation terms behave at least approximately as $1/x_2^+$ in the overlap region. [George and Castillo, 1997, Wosnik et al., 2000] argue from Near-Asymptotics that the dissipation in the overlap region of a channel or pipe flow varies as $1/x_2$; i.e., $\epsilon^+ = D/x_2^+$, where D depends weakly on $\ln \delta^+$ and is asymptotically constant. The result is exact for a parallel flow homogeneous in the streamwise direction. [George and Castillo, 1997] argue it is at least approximately true for zero-pressure gradient boundary layers even if it varies as a power law $\epsilon^+ \propto D_i/{x_2^+}^{1-\gamma}$ since γ is a small parameter which decreases with increasing $\ln \delta^+$. In figure 7, all

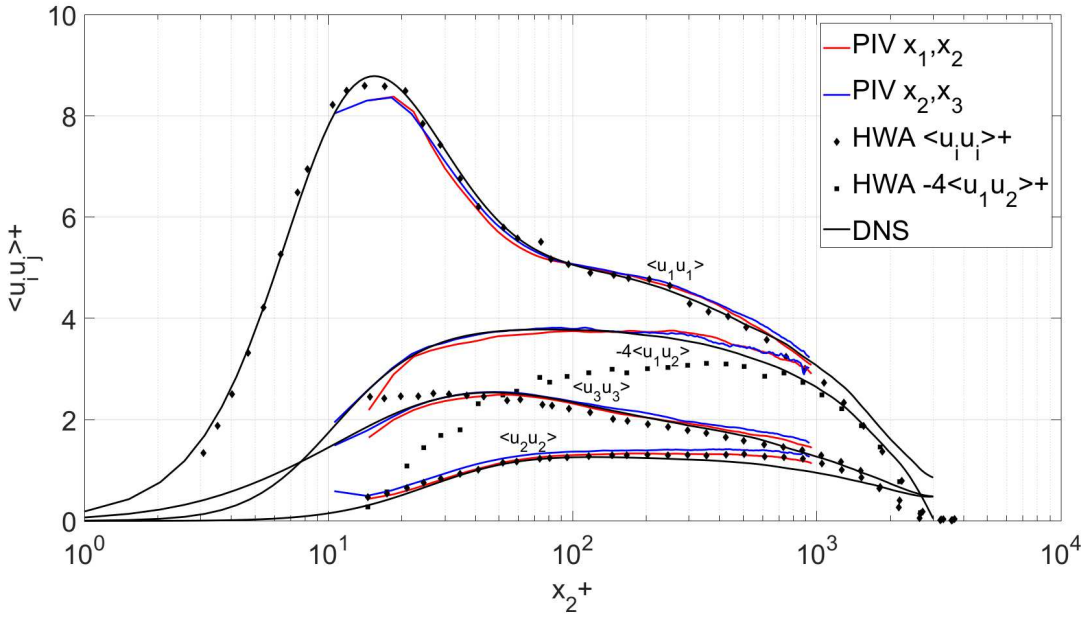

Figure 6: Turbulence intensity profiles of the two PIV planes compared to hot-wire of [Carlier and Stanislas, 2005] and DNS data of [Thais et al., 2011].

derivatives multiplied by x_2^+ are effectively nearly constant, but it is impossible to tell whether the power is exactly -1 or simply close to it. This is consistent with the arguments of [George and Castillo, 1997] that the overlap region of a boundary layers is slightly different from channel flow due to the streamwise inhomogeneity of the flow. For the mean velocity and turbulence velocity moments this implies weak power law profiles instead of logarithmic profiles.

5.3 Comparison with DNS and previous hot-wire results

Figures 8 and 9 show respectively the normal moments involving u_1 and the crossed derivative moments (The other moments comparisons are provided as supplementary material). These data are compared with the channel flow DNS described in section 3 and previous hot-wire measurements of [Balint et al., 1991] and [Honkan and Andreopoulos, 1997]. All data are premultiplied by x_2^+ to evidence the differences. Despite an underestimation of the near-wall peak by SPIV due to the lack of spatial resolution in this region, the agreement between the SPIV and the channel flow DNS is quite gratifying, notably for $\langle u_{1,1}u_{1,1}\rangle$ and $\langle u_{2,3}u_{3,2}\rangle$. This agreement is fairly good for the other moments for $y^+ > 500$. For several moments, a difference of behaviour is observed in the overlap region: the SPIV data appear relatively constant while the DNS data decrease slowly away from the wall. As will be seen later this is also observed for the dissipation. This phenomenon is attributed to the difference in flow nature between the SPIV boundary layer and the DNS channel flow.

The situation is not the same for the previous measurements of [Balint et al., 1991] and [Honkan and

Table 2: Summary showing how each squared derivative moment was obtained. Details on the corrections are given in Foucaut et al. [2021].

$\left\langle \frac{\partial u_i}{\partial x_j} \frac{\partial u_i}{\partial x_j} \right\rangle$	plane	cross-plane	noise-corrected	continuity
i = 1 j = 1	x_1x_2	no	yes	yes
i ≠ 1 j = 1	x_1x_2	no	yes	no
i = 2 j = 2	both	yes	yes	yes
i ≠ 2 j = 2	both	yes	yes	no
i = 3 j = 3	x_2x_3	no	yes	yes
i ≠ 3 j = 3	x_2x_3	no	yes	no

Andreopoulos, 1997]. For the variances, the results of [Balint et al., 1991] are in reasonable agreement with the DNS and the present data, except for $\langle u_{3,1}u_{3,1}\rangle$ (not shown) which is very low. The crossed derivative moments are quite far off. This underestimation of the variances could be due to the difference in Reynolds numbers (which is not that large), but more likely is a consequence of limitations of hot-wire techniques. Concerning the data of [Honkan and Andreopoulos, 1997] it appeared in the course of the preparation of this paper, that the ϵ values in [Honkan and Andreopoulos, 1997] were by error multiplied by 2 (this was confirmed by one of the authors). It was supposed here that the same error affects the individual variances (the crossed moments were not provided in [Honkan and Andreopoulos, 1997]), so all their moments were divided by 2. They then come globally much closer to the other data. As can be seen in figure 8, the agreement is quite good for $\langle u_{1,1}u_{1,1}\rangle$. It is also good for the other moments beyond $x_2^+ = 200$.

The agreement is good as well for all the moments not shown and provided as supplementary material figures. In any case, the hierarchy of the different variances is coherent with the other data (see extra material). Close to the wall the present SPIV results definitely underestimate the DNS derivative moments due to the spatial filtering of the smaller scales by the finite SPIV interrogation window (which is about $5\eta \times 5\eta$ in the present case). Farther away from the wall (outside $x_2^+ > 50$) the present results are in relatively good agreement with [Balint et al., 1991] for some of the moments. It is difficult to find an explanation for the discrepancies as the technique to calculate these derivatives from the multiwire probes data is quite different from the SPIV approach. It is also different for the two HWA data of [Balint et al., 1991] and [Honkan and Andreopoulos, 1997], but involves into both cases a combination of first order spatial and time derivatives with a Taylor hypothesis to convert them in streamwise derivatives. In the SPIV, all derivatives are computed spatially on a uniform grid and using an optimized derivative filter.

5.4 Dissipation and production

Figure 10 shows the dissipation and production rates from the SPIV and DNS, along with that of [Balint et al., 1991, Honkan and Andreopoulos, 1997, Andreopoulos and Honkan, 2001] [1]. The data are presented in linear-logarithmic plot, premultiplied by x_2^+. For the production term, which is based on the Reynolds stresses themselves, SPIV is in fairly good agreement with the DNS, and between $x_2^+ = 40$ and 200 with

[1]Note the dissipation data of [Andreopoulos and Honkan, 2001] have been divided by 2 since the data reported in the paper were in error. This is in agreement with a discussion with Prof. Andreopoulos.

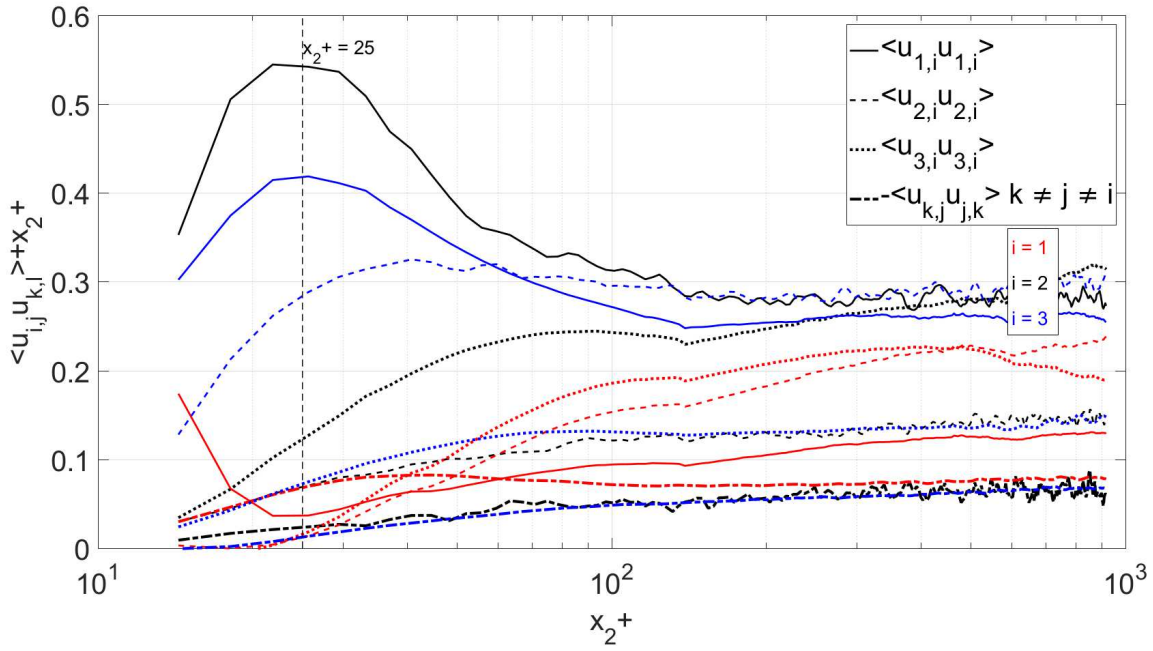

Figure 7: Linear-log plot of all the SPIV dissipation derivatives moments premultiplied by x_2^+ as a function of wall distance.

[Balint et al., 1991]. The data of [Honkan and Andreopoulos, 1997, Andreopoulos and Honkan, 2001] appear to underestimate the production near the wall and to overestimate it above $x_2^+ = 400$. This could possibly be attributed to a constant additive noise. For the dissipation, the SPIV data are in good agreement near the wall with the measurements of [Balint et al., 1991] and [Andreopoulos and Honkan, 2001], but all of them are below the DNS data for x_2^+ lower than about 200. This can be attributed to the difference in spatial resolution in the very near wall region. The nearly horizontal dissipation data from about $100 \leq x_2^+ \leq 800$ of both the SPIV and the [Honkan and Andreopoulos, 1997] data suggest a near $1/x_2^+$ behavior in this region. This result is somewhat supported by the DNS data of [Sillero et al., 2013] presented in figure 2. This will be discussed in detail below; but it is already interesting to note that in the same region, the DNS data for ϵ seem to depart slightly from this $1/x_2^+$ behavior.

It is commonly assumed that the near wall peaks mean that the near wall region dominates the overall dissipation for the boundary layer. That the opposite is true is clear from a linear-linear plot of the present data in figure 11. The long tail with increasing distance from the wall is the primary contributor to the integrated dissipation across the boundary layer. In fact since the near wall peak is fixed in inner variables, $x_2^+ = x_2 u_\tau/\nu$, while the tail is in outer variables, say x_2/δ_{99}, the relative contribution to the integral shifts progressively away from the wall as the Reynolds number increases (v. [George and Castillo, 1997]). At high Reynolds number the dissipation contribution to the boundary layer should be just an integral under the 'tail', most of which is in the overlap (or 'log') region.

Figure 12 shows a plot of the production and dissipation times x_2^+, along with a plot of the difference

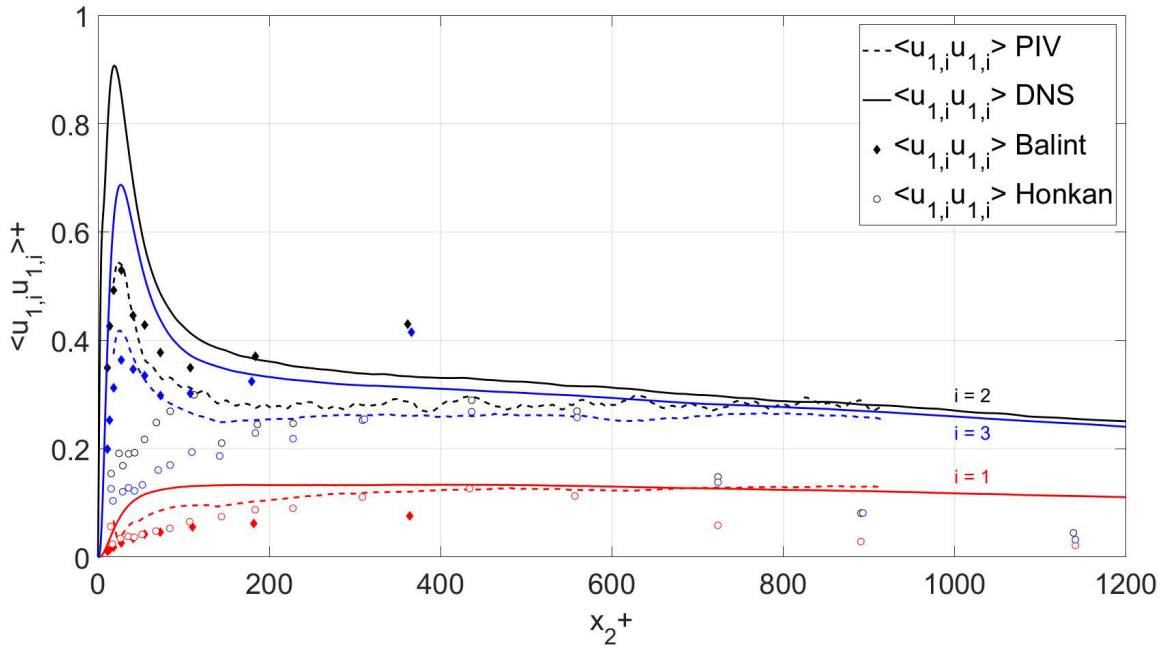

Figure 8: Comparison of SPIV derivative moments involving u_1 with DNS of [Thais et al., 2011] and hot-wire results of [Balint et al., 1991] and [Honkan and Andreopoulos, 1997].

$\epsilon^+ - \mathcal{P}^+$ (which is negative and corresponds to all the other terms of the transport equation for the Turbulence Kinetic Energy) as obtained from the boundary layer SPIV and channel DNS data. Looking first at the DNS, it is interesting to note that the peak of production is located at $x_2^+ = 15$, which is also the peak of TKE, while the peak of ϵ^+ is around $x_2^+ = 35$. The region where both terms are nearly equal is clearly visible and the difference (mostly diffusion) is nearly constant for $200 < x_2^+ < 800$. For SPIV, there is a larger difference between production and dissipation. Below $x_2^+ = 400$, part of it could be explained by the spatial filtering of PIV (corresponding to an interrogation window size WS in figure 4 larger than 3 Kolmogorov units). [Balint et al., 1991] also observed the same difference. They further noted that the suggestion of [Tennekes and Lumley, 1972] that production and dissipation should be equal in the overlap region seemed to be only approximately satisfied in their measurements. The only other term in the energy balance that could be significant in this region is the turbulence transport term. The slight deviation from horizontal of the production is most likely due to the need for a virtual origin to account for the mesolayer [George and Castillo, 1997, Wosnik et al., 2000]. Or that they should be described by a power-law slightly different from -1.

Figure 13 shows a similar plot for the channel DNS, this time in logarithmic representation. Two sets of data are provided: the present DNS data of [Thais et al., 2011] at $Re_\tau = 3000$ and the DNS of [Lee and Moser, 2015] at $Re_\tau = 5200$. Up to $x_2^+ = 600$, the general features are comparable to the boundary layer experimental data, and again there is about a 10% discrepancy. But here the difference is definitely

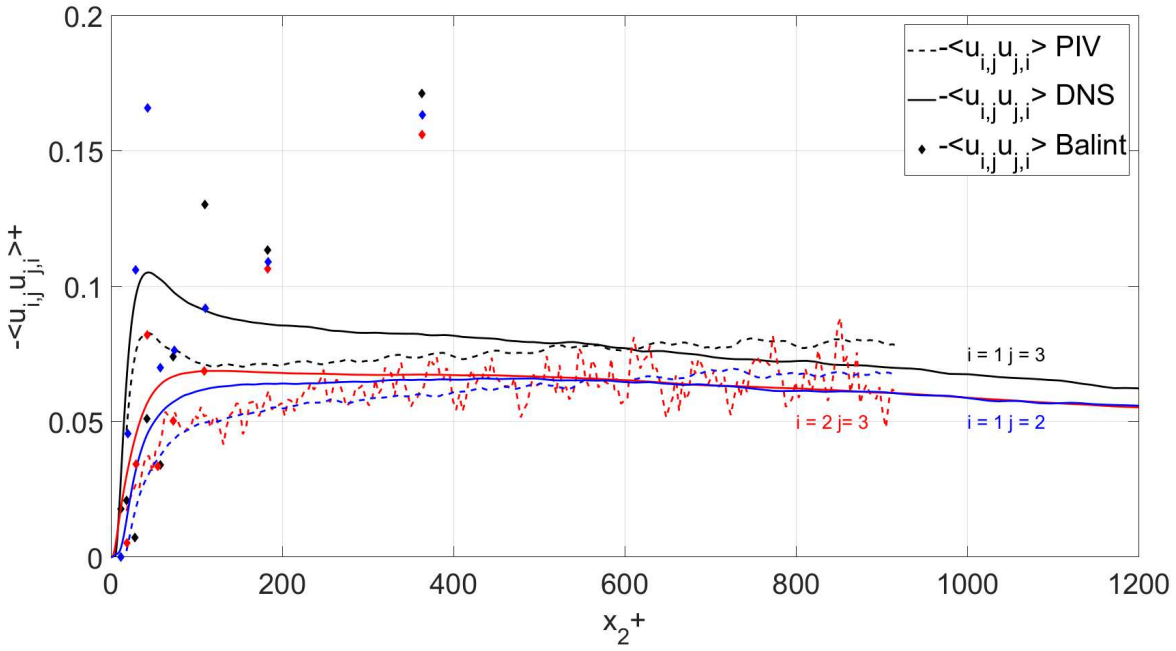

Figure 9: Comparison of SPIV derivative cross-products with channel DNS of [Thais et al., 2011] and hot-wire results of [Balint et al., 1991] and [Honkan and Andreopoulos, 1997].

due to transport terms in the energy balance equation. Above $x_2^+ = 600$, the behavior of the channel data changes significantly from the boundary layer. It is difficult to draw some definite conclusions as the boundary layer data extend only up to $x_2^+ = 1000$. If confirmed further away from the wall, this is most likely evidence of a different physics between the boundary layer and channel in the outerpart as seems to be supported by the DNS data of figure 2. It is of interest to note the effect of the Reynolds number between the two DNS which show a very similar behaviour and support the idea of a nearly $1/x_2$ behaviour of both production and dissipation in the overlap region when the Reynolds number is high enough. This idea is also supported by [Smits and Marusic, 2011] in their figure 1.

It is easy to extend the Near-Asymptotic analysis of [George and Castillo, 1997] to the transport terms. For example, for a streamwise homogeneous flow, they can be shown to be logarithmic; i.e.,

$$\langle -\frac{1}{2} u_i u_i u_j \rangle^+ - \frac{1}{\rho} \langle p u_j \rangle^+ + 2\nu \langle u_i s_{ij} \rangle^+ = T \; ln \; x_2^+ + S. \tag{11}$$

where T and S are related to the logarithmic profile counterparts of the velocity profile. As a result, the derivative in the wall normal direction is $1/x_2^+$, exactly as observed in figure 2. In the overlap region of a channel flow the mean convection terms of the equation for the turbulent kinetic energy are exactly zero and the viscous terms are negligible, so the overall energy balance reduces to just

$$0 = \frac{d}{dx_2^+} \left\{ -\frac{1}{2} \langle u_i u_i u_j \rangle^+ - \frac{1}{\rho} \langle p u_j \rangle^+ + 2\nu \langle u_i s_{ij} \rangle^+ \right\} - \langle uv \rangle^+ \frac{dU^+}{dx_2^+} - \epsilon^+ \tag{12}$$

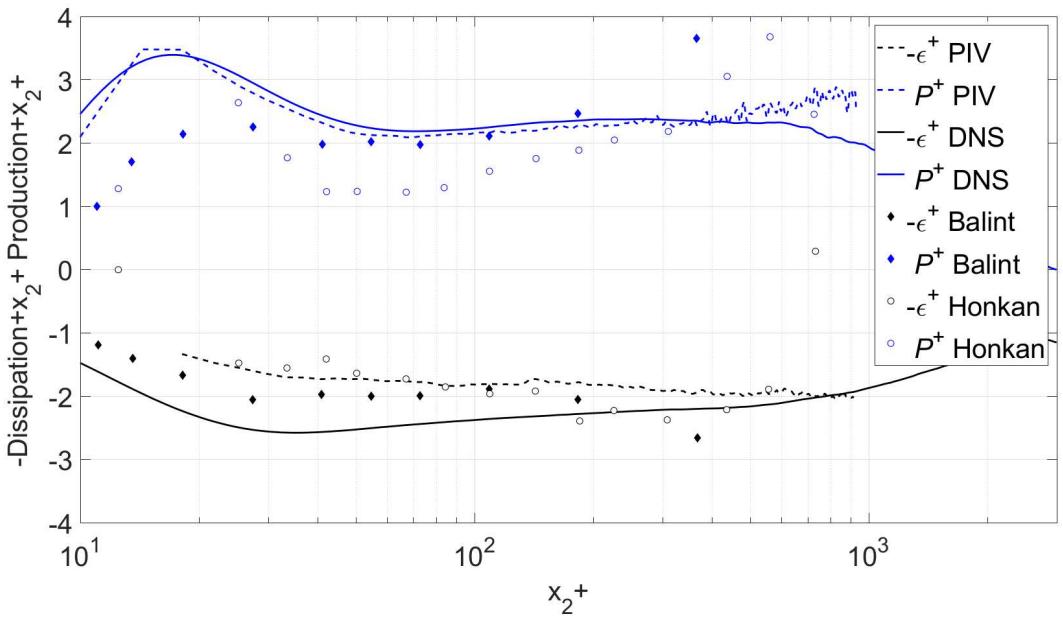

Figure 10: The dissipation rate ϵ and production rate in inner variables (linear-logarithmic) for DNS ([Thais et al., 2011]) and SPIV along with [Balint et al., 1991, Andreopoulos and Honkan, 2001]. The data are pre-multiplied by x_2^+.

But, at high Reynolds number, in inner variables (i.e., normalized by u_τ and ν), $-\langle uv\rangle^+ = 1$ and $dU^+/dx_2^+ = 1/\kappa$ (where κ is the Von-Karman parameter), so it follows immediately that ALL the surviving terms in the overlap region vary as $1/x_2^+$, and $0 = T + (1/\kappa) - D$.

For the boundary layer, these same transport terms vary as a weak power law for a streamwise developing flow; i.e,

$$-\langle\frac{1}{2}u_iu_iu_j\rangle^+ - \langle\frac{1}{\rho}pu_j\rangle^+ + 2\nu\langle u_is_{ij}\rangle^+ = T_ix_2^{+\beta} \tag{13}$$

and the same conclusions can be drawn.

6 Local isotropy

By far the most common assumption by all experimenters has been the assumption of *local isotropy*, an idea originally introduced by [Taylor, 1935]. (Note that the deductions from the *local isotropy* hypothesis are often confused with implications from just continuity and *local homogeneity* as noted by [George and Hussein, 1991].) When applied to velocity derivatives, *local isotropy* demands that all mean square

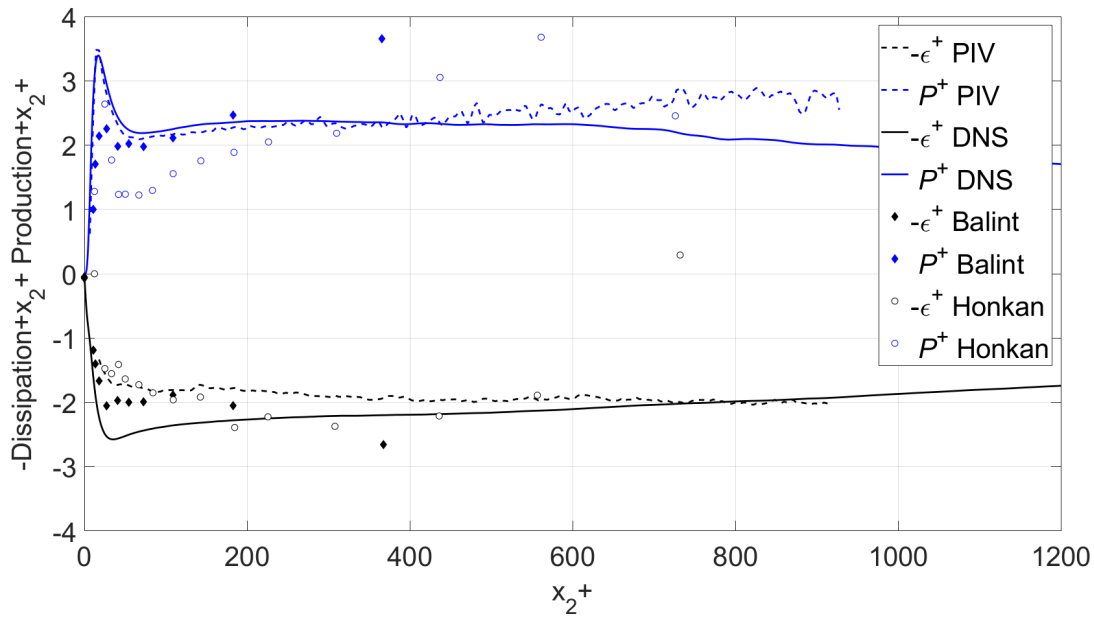

Figure 11: The dissipation rate ϵ and production rate in inner variables (linear-linear) for DNS ([Thais et al., 2011]) and SPIV along with [Balint et al., 1991, Andreopoulos and Honkan, 2001]. The data are pre-multiplied by x_2^+.

derivatives obey the isotropic relations; in particular:

$$\langle\left[\frac{\partial u_1}{\partial x_1}\right]^2\rangle = \langle\left[\frac{\partial u_2}{\partial x_2}\right]^2\rangle = \langle\left[\frac{\partial u_3}{\partial x_3}\right]^2\rangle \tag{14}$$

$$\langle\left[\frac{\partial u_1}{\partial x_2}\right]^2\rangle = \langle\left[\frac{\partial u_2}{\partial x_1}\right]^2\rangle = \langle\left[\frac{\partial u_1}{\partial x_3}\right]^2\rangle = \langle\left[\frac{\partial u_3}{\partial x_1}\right]^2\rangle \tag{15}$$

$$= \langle\left[\frac{\partial u_2}{\partial x_3}\right]^2\rangle = \langle\left[\frac{\partial u_3}{\partial x_2}\right]^2\rangle = 2\langle\left[\frac{\partial u_1}{\partial x_1}\right]^2\rangle \tag{16}$$

$$\langle\left[\frac{\partial u_1}{\partial x_2}\frac{\partial u_2}{\partial x_1}\right]\rangle = \langle\left[\frac{\partial u_1}{\partial x_3}\frac{\partial u_3}{\partial x_1}\right]\rangle = \langle\left[\frac{\partial u_2}{\partial x_3}\frac{\partial u_3}{\partial x_2}\right]\rangle = -\frac{1}{2}\langle\left[\frac{\partial u_1}{\partial x_1}\right]^2\rangle \tag{17}$$

Consequently, for local isotropy, there is only one-independent derivative moment so any one can be chosen. The two most popular reduce the dissipation to:

$$\epsilon = 15\nu\langle\left[\frac{\partial u_1}{\partial x_1}\right]^2\rangle = \frac{15}{2}\nu\langle\left[\frac{\partial u_2}{\partial x_1}\right]^2\rangle. \tag{18}$$

Results of both (usually obtained using Taylor's hypothesis) are often cited side-by-side in the literature, even though they often yield very different answers. [Antonia et al., 1986, 1991] tabulate results from a

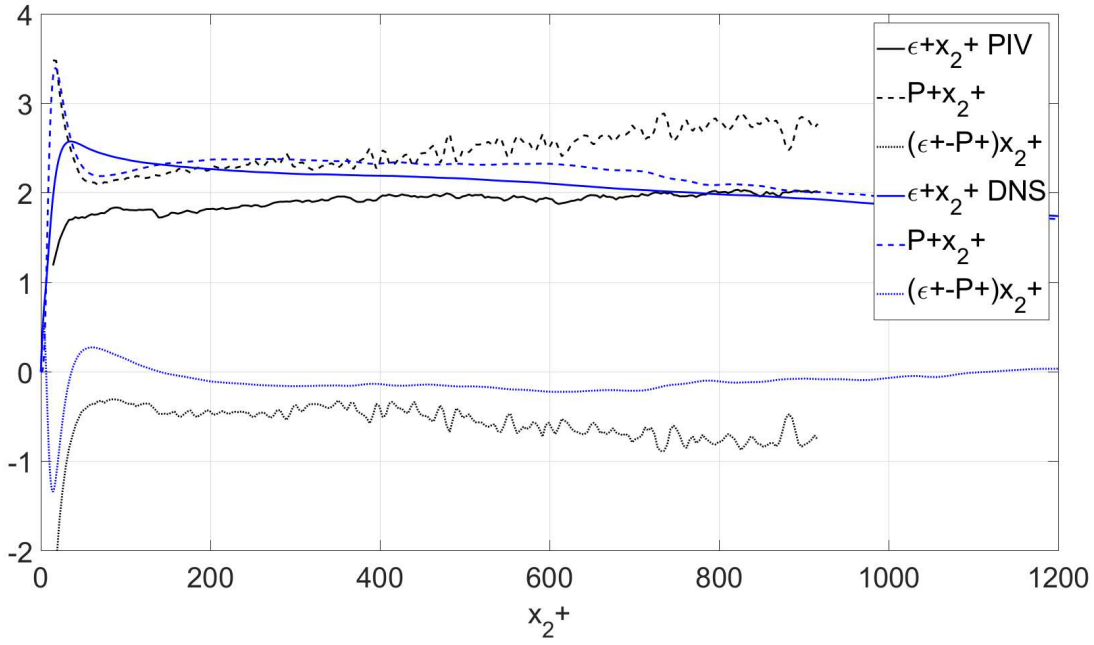

Figure 12: Linear plot of the SPIV energy balance premultiplied by x_2 in inner variables; i.e., production, $P^+ = x_2^+ \langle uv \rangle^+ dU^+/dx_2^+$ (broken), dissipation $x_2^+ \epsilon^+$ (plain) and difference between these two terms $(\epsilon^+ - P^+)x_2^+$.

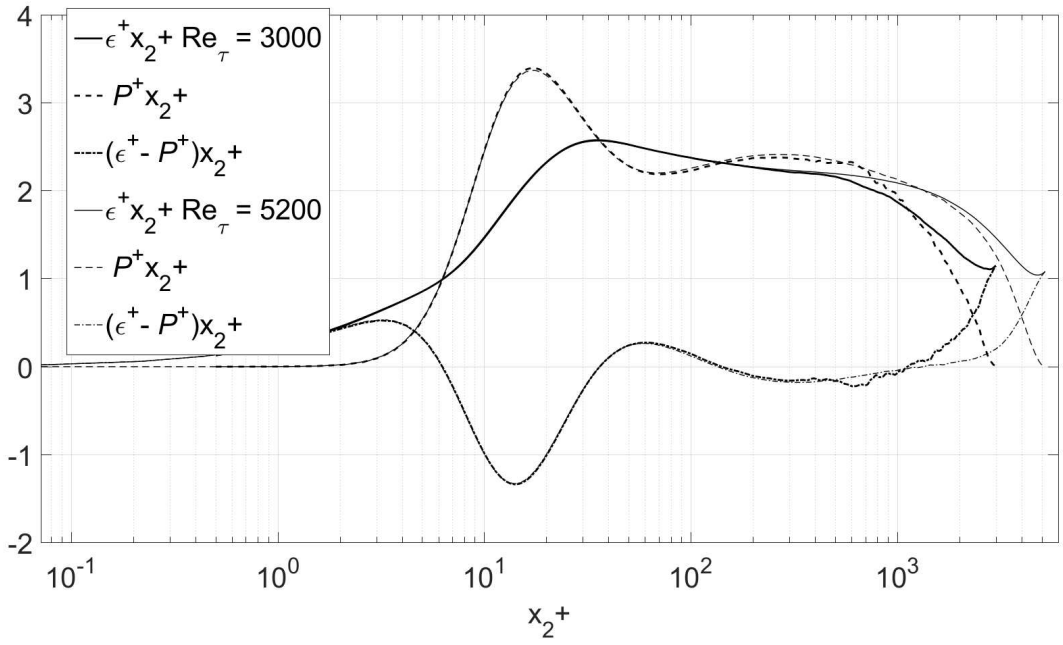

Figure 13: Logarithmic plot of the DNS energy balance premultiplied by x_2 in inner variables; i.e., production, $\langle uv \rangle^+ dU^+/dx_2^+$ (broken), dissipation $x_2^+ \epsilon^+$ (plain) and difference between these two terms (dotted), for two values of the Reynolds number by [Thais et al., 2011] at $Re_\tau = 3000$ and [Lee and Moser, 2015] at $Re_\tau = 5200$.

large number of flows, almost none of which are consistent with the *local isotropy* assumption (see also [George and Hussein, 1991]). Nonetheless, this *local isotropy* assumption is still widely used, mostly for the lack of easy alternatives. A certain amount of luck would be required to obtain a reasonable estimate from the measurement of a single derivative, especially when the Taylor hypothesis of frozen turbulence is used as well.

Figure 14 gives some of the SPIV derivative moments in inner variables multiplied by x_2^+ in semi-log plots. The data have been plotted in groups (a) to (d) to show the expected equalities of equations (14-17), and multiplied by the appropriate factors to make them equal if the flow were *locally isotropic*. Figure 15 shows a more global plot with all the moments from the DNS data. Note that inside of $x_2^+ = 30$ the experimental data are affected by the limited spatial resolution, but the DNS data are not. And note also that the channel flow DNS data extend to the center of the channel, while the boundary layer data extend only till about $x_2/\delta_{0.99} = 0.4$, which is near the outer limit of the overlap (or log) region.

Inside of $x_2^+ = 100$, the departures from isotropy are catastrophic. The anisotropy very close the wall ($x_2^+ < 5$) can be explained by a simple Taylor expansion of the variables there, since the continuity equation together with the boundary conditions dictates the behavior in that region. This has already been discussed extensively by DNS and turbulence modellers [Manceau et al., 2002], [Gerolymos and Vallet, 2016]. Outside of $x_2^+ = 100$, the departures from isotropy for both sets of data are on the order of

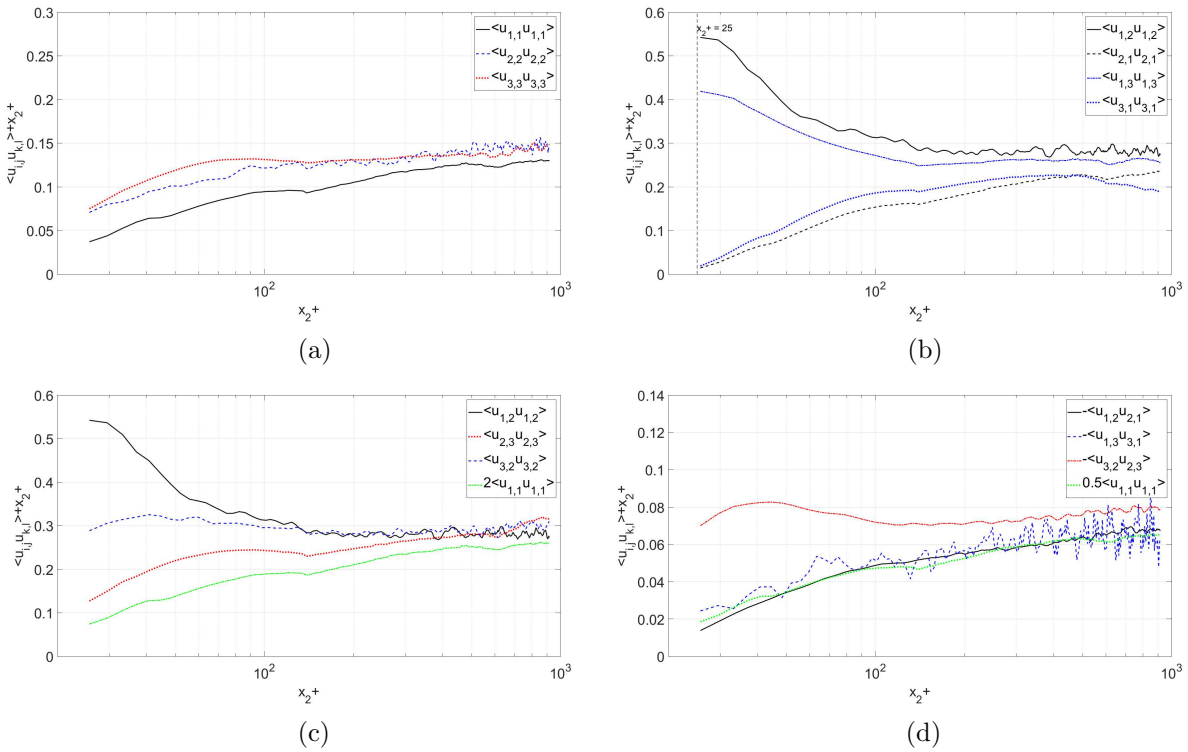

Figure 14: Isotropy test of SPIV data. (a) eq. (14), (b) eq. (15), (c) eq. (16), (d) eq. (17). Note that ordinates have been multiplied by x_2^+.

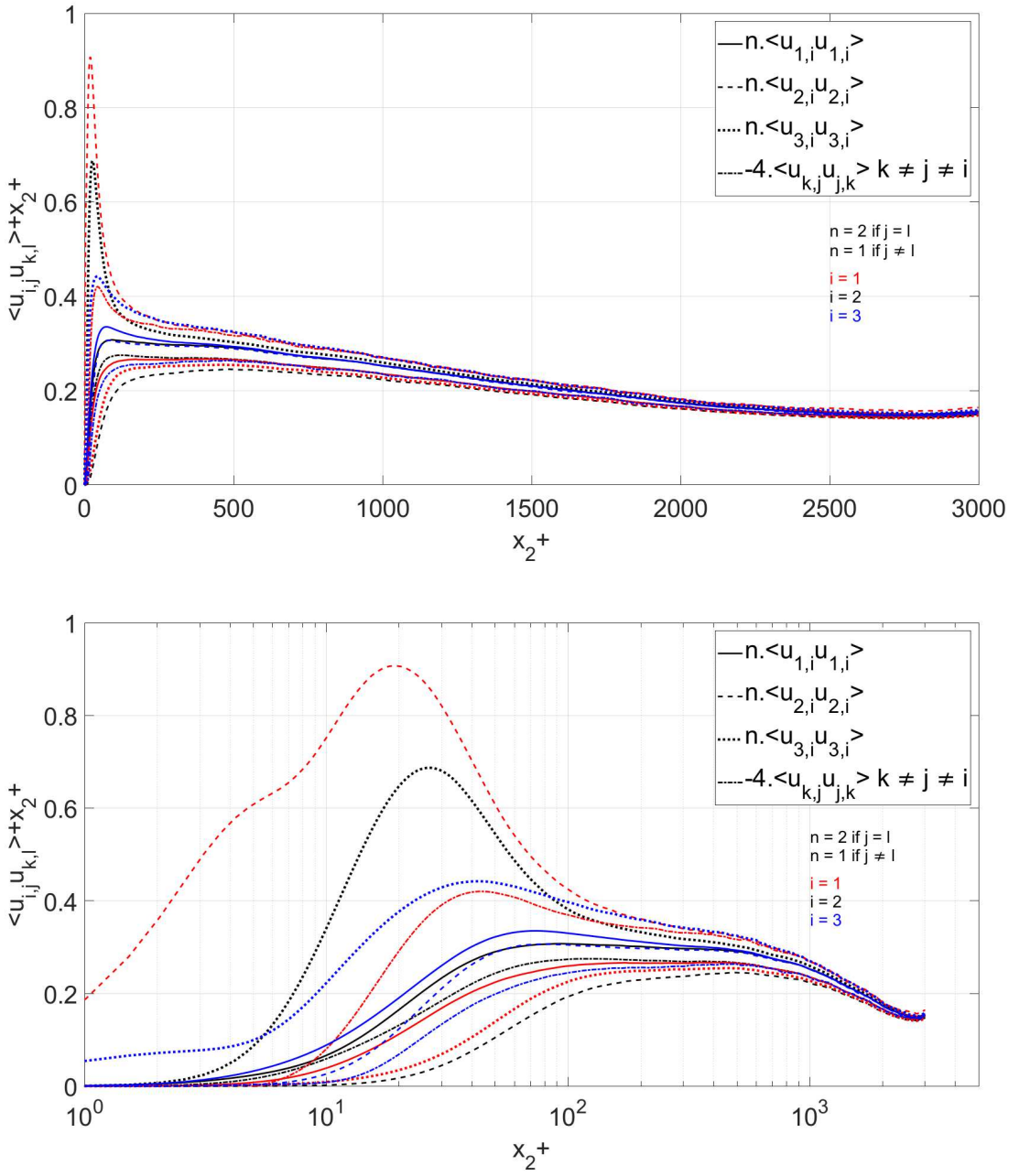

Figure 15: Isotropy test of [Thais et al., 2011] DNS data. See equations (14-17). Note that ordinates have been multiplied by x_2^+.

50% or more, at least throughout the overlap region. The channel flow data shows some tendency toward isotropy in the core region ($x_2^+ > 1000$ or so), but no definite assessment can be made for the boundary layer outside of the overlap region.

So local isotropy is clearly a very bad assumption for this boundary layer flow everywhere, at least within the overlap region and below. As they are relevant mostly below $x_2^+ = 100$, the anisotropy diagrams for the dissipation tensors will be presented and discussed in Section 9 below, and will be seen to show the same characteristics. In any case, as can be seen in figures 14 and 15, the streamwise mean square derivative, $\langle[\partial u_1/\partial x_1]^2\rangle$, is a particularly bad representative of the rest. This is unfortunate since it has been historically most commonly used with time derivatives and Taylor's hypothesis to estimate dissipation in all flows.

Whether the smallest scales of motion themselves are isotropic is another matter which cannot be resolved with the current data. As noted above, this is a separate question from whether the isotropic derivative relations are approximately satisfied.[2] Perhaps at higher Reynolds numbers the core region of the channel will tend toward isotropy – say outside of $x_2^+ > 0.1H^+$. This would be consistent with the spectral suggestions of [George and Castillo, 1997] and the observations of [George and Tutkun, 2011] (using measurements at higher Reynolds number in the same Lille facility) that the outer part of the boundary layer only reaches a true multi-point Reynolds number independence when $\delta^+ > 3000$ approximately, and even then only for $x_2^+ > 0.1\delta^+$. When these conditions are not satisfied, all scales of motion are affected by viscosity, so any Kolmogorov 41 type arguments simply cannot apply – including any tendency toward isotropy and an inertial range in the energy spectra (or structure functions).

7 Local axisymmetry

The theory of axisymmetric turbulence was developed in parallel using different methodologies by [Batchelor, 1954] and [Chandrasekar, 1950]. But it was [George and Hussein, 1991] who realized its potential applicability to the turbulence derivative moments and coined the term *local axisymmetry*. And [Antonia et al., 1991] were the first to apply these ideas to turbulent wall-bounded flows. One important condition, put forward by [George and Hussein, 1991], is that *local homogeneity* is necessary for *local axisymmetry* to exist. Note that the whole idea of *local* in this context is that the axisymmetric relations only apply to quantities dominated by the smallest scales of motion. So the axisymmetric relations presented below only apply to the derivative moments, not to the velocity moments in general. [George and Hussein, 1991] only developed the equations for an axis of symmetry which corresponded to the 1-axis. (Other orthogonal orientations can be obtained by simply permuting the preferred axis-1 with a different axis.) It was not obvious to them why the 1-axis should have been preferred, nor is it now. But the data seemed to suggest strongly that the derivative moments arrange into pairs (with always one single exception). Thus *local axisymmetry* (with the 1-axis as preferred) requires:

[2]The measurements of [Saddoughi and Veeravalli, 1994] show that spectra from a very high Reynolds number at NASA/Ames agree reasonably well with the isotropic spectral relations at high wavenumbers. In the absence of anisotropic spectral relations, however, this does not constitute proof, since the anisotropic contributions to the spectral relations could be negligible. This is especially problematical since the anisotropy of the intensities in their experiment is only about 20% or less.

$$
\begin{aligned}
\langle\left[\frac{\partial u_1}{\partial x_2}\right]^2\rangle &= \langle\left[\frac{\partial u_1}{\partial x_3}\right]^2\rangle & \langle\left[\frac{\partial u_2}{\partial x_1}\right]^2\rangle &= \langle\left[\frac{\partial u_3}{\partial x_1}\right]^2\rangle \\
\langle\left[\frac{\partial u_2}{\partial x_2}\right]^2\rangle &= \langle\left[\frac{\partial u_3}{\partial x_3}\right]^2\rangle & \langle\left[\frac{\partial u_2}{\partial x_3}\right]^2\rangle &= \langle\left[\frac{\partial u_3}{\partial x_2}\right]^2\rangle \\
\langle\left[\frac{\partial u_2}{\partial x_2}\right]^2\rangle &= \frac{1}{3}\langle\left[\frac{\partial u_1}{\partial x_1}\right]^2\rangle + \frac{1}{3}\langle\left[\frac{\partial u_2}{\partial x_3}\right]^2\rangle & & \\
\langle\left[\frac{\partial u_2}{\partial x_3}\frac{\partial u_3}{\partial x_2}\right]\rangle &= \frac{1}{6}\langle\left[\frac{\partial u_1}{\partial x_1}\right]^2\rangle - \frac{1}{3}\langle\left[\frac{\partial u_2}{\partial x_3}\right]^2\rangle & & \\
\langle\left[\frac{\partial u_1}{\partial x_2}\frac{\partial u_2}{\partial x_1}\right]\rangle &= \langle\left[\frac{\partial u_1}{\partial x_3}\frac{\partial u_3}{\partial x_1}\right]\rangle = -\frac{1}{2}\langle\left[\frac{\partial u_1}{\partial x_1}\right]^2\rangle & &
\end{aligned}
\tag{19}
$$

All of the above relations, which can be referenced as a (5x2) matrix, can be and have been checked across the boundary layer using the data presented herein. Figure 16 shows some of them for SPIV and DNS data (the others are in the supplementary material). Interestingly all appear to satisfy these relations outside of $x_2^+ > 100$ to an excellent approximation and some stay valid down to the wall. In fact they fail near the wall about the same place as *local homogeneity* fails (as will be shown below).

It is important to note that [George and Hussein, 1991] pointed out that if the velocity derivative moments were strictly axisymmetric, then there could be no enstrophy (or dissipation) production direct from the mean shear, similar to the degeneracy of isotropy. So at least one derivative moment must not satisfy the axisymmetric relations – as in fact observed in figure 16 which shows that two relations are more approximate in the outer part and clearly fail below $x_2^+ = 100$. As we shall see below, *local homogeneity* breaks down about the same place, so the point appears to be moot. Interestingly it is the equality involving the 2-3 derivative which fails most near the wall. It is the same derivative which dominates the vorticity amplification of streamwise vorticity. The present data appear to give strong support for the hypothesis of *local axisymmetry* outside of $x_2^+ = 100$.

Inside $x_2^+ = 100$, is a different story. *Both local axisymmetry* and *local isotropy* fail. As noted above, the anisotropy diagrams presented in Section 9.3 below exhibit the same behavior. The reason for the failure of both inside $x_2^+ = 100$ will be obvious in the next section, and seen to be due to a complete failure of *local homogeneity* in this region, without which neither can be true.

In any case, a clear advantage of *local axisymmetry* is that only four derivative moments are independent, and they can be chosen for convenience. Of the many combinations possible, [George and Hussein, 1991] suggested and used two for the dissipation; namely,

$$
\epsilon \simeq \nu\left\{\langle-\left[\frac{\partial u_1}{\partial x_1}\right]^2\rangle + 8\langle\left[\frac{\partial u_2}{\partial x_2}\right]^2\rangle + 2\langle\left[\frac{\partial u_1}{\partial x_2}\right]^2\rangle + 2\langle\left[\frac{\partial u_2}{\partial x_1}\right]^2\rangle\right\} \tag{20}
$$

and

$$
\epsilon \simeq \nu\left\{\frac{5}{3}\langle\left[\frac{\partial u_1}{\partial x_1}\right]^2\rangle + 2\langle\left[\frac{\partial u_1}{\partial x_2}\right]^2\rangle + 2\langle\left[\frac{\partial u_2}{\partial x_1}\right]^2\rangle + \frac{8}{3}\langle\left[\frac{\partial u_2}{\partial x_3}\right]^2\rangle\right\}. \tag{21}
$$

The first of these lends itself naturally to measurements in a plane (like planar PIV), but to our knowledge has not previously been used this way. The second is most useful for the particular configuration of

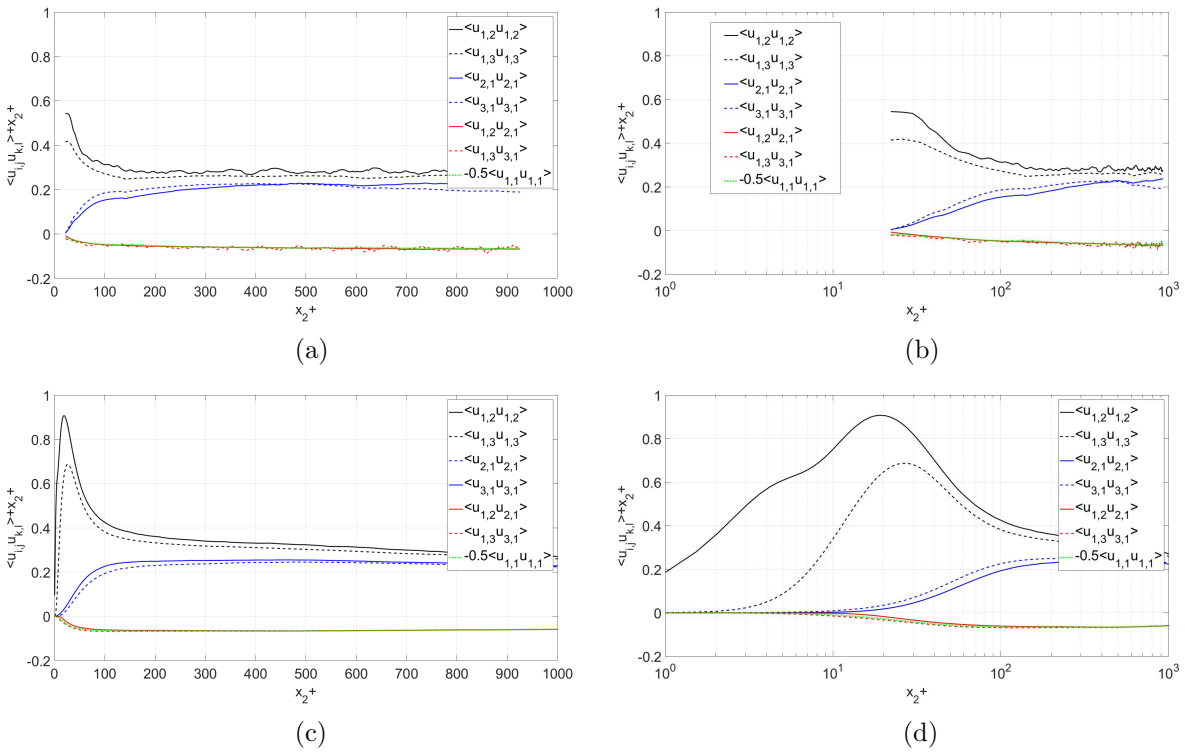

Figure 16: Axisymmetry test of derivative moments from SPIV ((a) & (b)) and [Thais et al., 2011] DNS ((c) & (d)) in both lin-lin ((a) & (c)) and lin-log plots ((b) & (d)). See equations (19): Black corresponds to equation (1,1); blue to equation (1,2); red to equation (5,1) and green and red to equation (5,2). Note that ordinates have been multiplied by x_2^+.

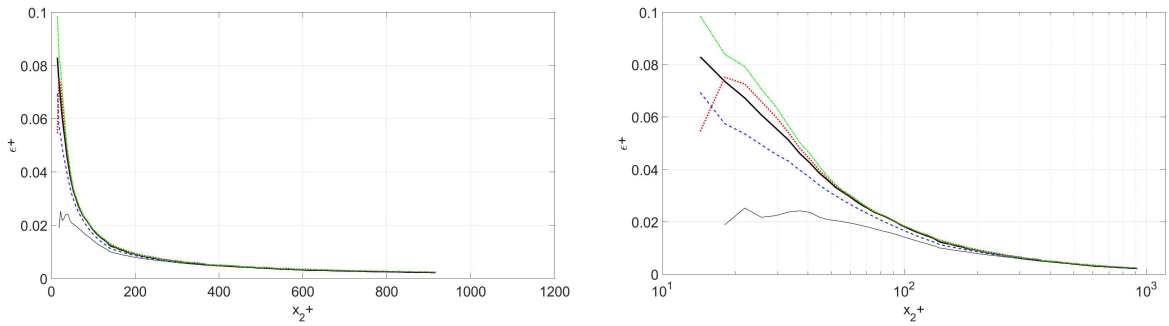

Figure 17: Validation of the estimation of the full dissipation (thick black) by the approximate equations (20) in red, (21) in blue and (22) in green based on local axisymmetry and on equation 18 for local isotropy in thin black.

parallel x-wires which can be rotated by 90 degrees. Another possibility, suited for SPIV measurements in a streamwise plane writes:

$$\epsilon \simeq \nu \left\{ \frac{7}{3} \langle \left[\frac{\partial u_1}{\partial x_1} \right]^2 \rangle + 4 \langle \left[\frac{\partial u_2}{\partial x_2} \right]^2 \rangle + 2 \langle \left[\frac{\partial u_1}{\partial x_2} \right]^2 \rangle + 2 \langle \left[\frac{\partial u_2}{\partial x_1} \right]^2 \rangle \right\} + \nu \left\{ \frac{4}{3} \langle \left[\frac{\partial u_3}{\partial x_2} \right]^2 \rangle + 4 \langle \frac{\partial u_1}{\partial x_2} \frac{\partial u_2}{\partial x_1} \rangle \right\} \tag{22}$$

Figure 17 gives a comparison of the three above estimates with the full dissipation for the SPIV data. The first estimate of equation (20) works well right to the wall because of cancellation of different terms in the sum (some derivatives which are too large are compensated by those which are too small). As noted by [Antonia et al., 1991] and more recently by [Zhao et al., 2015] as well, the second one (equation (21)) fails inside of $x_2^+ = 200$. The last proposal (equation (22)) is fairly good down to $x_2^+ = 50$, and then gives a slight overestimation. [3]

8 Local homogeneity

As it will be at the heart of the following discussions, it is worth to mention already here that an important consequence of the hypothesis of *homogenous* turbulence is that the indices of derivative moments such as those appearing in the equations for the dissipation tensor can be permuted; i.e.,

$$\langle \frac{\partial u_i}{\partial x_m} \frac{\partial u_j}{\partial x_n} \rangle = \langle \frac{\partial u_i}{\partial x_n} \frac{\partial u_j}{\partial x_m} \rangle \tag{23}$$

[3] In a recent paper, [Zaripov et al., 2019] apply equation (20) to high speed planar PIV. The results shown in their figure 13 confirm the present results of figure 17 and the benefit brought by these axisymmetric formula for the estimation of the dissipation in PIV experiments.

If the flow is also incompressible, then it follows immediately that

$$\langle \frac{\partial u_i}{\partial x_j} \frac{\partial u_j}{\partial x_i} \rangle = \langle \frac{\partial u_i}{\partial x_i} \frac{\partial u_j}{\partial x_j} \rangle = 0 \tag{24}$$

which cancels the cross products appearing at the right of the equations for the dissipation tensor and scalar dissipation. The immediate consequence is that in homogeneous incompressible turbulence both $\mathcal{D}_{ij} = \epsilon_{ij}$ and $\mathcal{D} = \epsilon$. This is more general than the fact that the cross-products simplify themselves between the dissipation and the viscous diffusion in the equations for the Reynolds stresses and for the Turbulence Kinetic Energy. Here both are zero.

The basic ideas behind *local homogeneity* were first introduced by [Taylor, 1935], although he did not identify them as such. So these results were often confused with his conclusions from *local isotropy*, at least until [George and Hussein, 1991].[4]

8.1 What is local homogeneity

The very idea of *local homogeneity* as been at the core of turbulence thinking since the beginning of modern turbulence theory (c.f [Taylor, 1935, Kolmogorov, 1941]), and was the rationale behind applying spectral and structure function relations to the smallest scales of inhomogeneous flows. Curiously while the phrase *local isotropy* is in common use since [Batchelor, 1953], to the best of our knowledge the actual term *local homogeneity* appears to have first been introduced by [George and Hussein, 1991]. As with *local isotropy* and local *axisymmetry*, the whole idea of *local homogeneity* is that it only applies to statistical quantities dominated by the smallest scales of motion – in this context the derivative moments. Thus transport terms need not be zero, and only the derivative moment relations of equations (23) need apply. This leads to the following relevant equalities:

$$\begin{array}{lll}
\langle \frac{\partial u_1}{\partial x_1} \frac{\partial u_2}{\partial x_2} \rangle = \langle \frac{\partial u_1}{\partial x_2} \frac{\partial u_2}{\partial x_1} \rangle & \langle \frac{\partial u_1}{\partial x_1} \frac{\partial u_2}{\partial x_3} \rangle = \langle \frac{\partial u_1}{\partial x_3} \frac{\partial u_2}{\partial x_1} \rangle & \langle \frac{\partial u_1}{\partial x_2} \frac{\partial u_2}{\partial x_3} \rangle = \langle \frac{\partial u_1}{\partial x_3} \frac{\partial u_2}{\partial x_2} \rangle \\
\langle \frac{\partial u_1}{\partial x_1} \frac{\partial u_3}{\partial x_2} \rangle = \langle \frac{\partial u_1}{\partial x_2} \frac{\partial u_3}{\partial x_1} \rangle & \langle \frac{\partial u_1}{\partial x_1} \frac{\partial u_3}{\partial x_3} \rangle = \langle \frac{\partial u_1}{\partial x_3} \frac{\partial u_3}{\partial x_1} \rangle & \langle \frac{\partial u_1}{\partial x_2} \frac{\partial u_3}{\partial x_3} \rangle = \langle \frac{\partial u_1}{\partial x_3} \frac{\partial u_3}{\partial x_2} \rangle \\
\langle \frac{\partial u_2}{\partial x_1} \frac{\partial u_3}{\partial x_2} \rangle = \langle \frac{\partial u_2}{\partial x_2} \frac{\partial u_3}{\partial x_1} \rangle & \langle \frac{\partial u_2}{\partial x_1} \frac{\partial u_3}{\partial x_3} \rangle = \langle \frac{\partial u_2}{\partial x_3} \frac{\partial u_3}{\partial x_1} \rangle & \langle \frac{\partial u_2}{\partial x_2} \frac{\partial u_3}{\partial x_3} \rangle = \langle \frac{\partial u_2}{\partial x_3} \frac{\partial u_3}{\partial x_2} \rangle
\end{array} \tag{25}$$

It has been noted already that, thanks to equation (24), an immediate consequence of *local homogeneity* and incompressibility is that $\mathcal{D}$ as defined by equation (4) is equal to the true dissipation, ϵ as given by equation (3). For clarity $\mathcal{D}$ has been referred to by [George and Hussein, 1991] as the *pseudo-dissipation* or by others as the *homogeneous dissipation*. Some have erroneously construed this to mean that $\mathcal{D}$ is somehow more fundamental than ϵ. Nothing could be further from the truth: ϵ is *always* the true dissipation. $\mathcal{D}$ only equals it in a homogeneous flow, and contains other terms involving rotation when the flow is not homogenous. Another consequence of homogeneity is that the mean square strain-rate and mean square rotation rates are equal; i.e., $\langle \omega_{ij} \omega_{ij} \rangle = 2 \langle s_{ij} s_{ij} \rangle$.

[4] Taylor's long forgotten results were independently rederived by George and Hussain [George and Hussein, 1991], and they coined the phrase *locally homogeneous*, at least in the context of turbulence derivatives. Most turbulence models previously thought to depend on *local isotropy* or an isotropic dissipation assumption, in fact needed only local homogeneity.

8.2 Tests of local homogeneity from experiment and DNS

The large number of derivative moment combinations available in the present experiments and DNS makes it possible to exhaustively test the *local homogeneity* hypothesis provided by equations (25), even for derivative combinations which do not appear in either the dissipation or the enstrophy.

Figures 18 shows plots of the various pairs of cross-derivative moments from the BL experiment and channel DNS, which should fulfill equations (25) if the turbulence can be considered *locally homogeneous*. To help identification, equations (25) are considered here as a (3x3) matrix of equalities which are referred to in the legend of the figure. The close correspondence of the derivative pairs outside of $x_2^+ = 100$ is truly remarkable. Figure 18 also makes it clear that the derivative combinations which do not appear in either the dissipation or the enstrophy are in a range more than an order of magnitude smaller. A careful analysis shows that they also fullfill the *local homogeneity* condition in the overlap region. The general conclusion is then that outside of $x_2^+ = 100$, *local homogeneity* is an excellent approximation.

Consequently, the full dissipation ϵ and the pseudo-dissipation $\mathcal{D}$ should be very close in this region. This is verified in figure 19 which provides both ϵ and $\mathcal{D}$ from the SPIV data. As can be seen, the difference is hardly visible between the two terms, confirming the validity of the local homogeneity hypothesis in the overlap and outer regions of the boundary layer.

Inside of $x_2^+ = 100$ is a different story. Note that only the DNS channel data are reliable in this region. Looking at figure 18 and at equations 25, not only are equations (2,3) and (3,3) not satisfied but all these terms should be zero due to incompressibility.

As mentionned earlier, the absence of *local homogeneity* inside of $x_2^+ = 100$ eliminates any possibility of eventual *local axisymmetry* or local isotropy. This is a matter of concern as under such conditions we cannot expect to have $\epsilon_{ij} = \mathcal{D}_{ij}$. This fact is adressed in more detail in the next section.

9 Dissipation in the near wall region $x_2^+ < 100$

All of our experimental and DNS data provide overwhelming evidence that the conditions for *local homogeneity* are not met even approximately inside of $x_2^+ = 100$. Yet, as assumed by most of the turbulence community, the present data seem to indicate that $\mathcal{D} \approx \epsilon$, even close to the wall. The question which rises immediately is whether any other hypothesis exists which can explain what is happening in this very near wall region.

9.1 The near wall data

To answer this question we examine first the shape of the dissipation tensor ϵ_{ij}. Figure 20 gives a lin-log plot of the main components of this tensor in the near wall region. Data are compared from the SPIV boundary layer experiment, the present channel DNS of [Thais et al., 2011] and the Boundary Layer DNS of [Sillero et al., 2013]. The top figure gives the ϵ_{11} and ϵ_{33} diagonal terms and the bottom one ϵ_{22} and the main cross-term ϵ_{12}. The first thing to notice is that the cross-term ϵ_{12} is negative (consistent with the fact that $\langle u_1 u_2 \rangle$ is also negative) and an order of magnitude smaller than the diagonal terms, except for ϵ_{33}. This cross-term is in fairly good agreement with the data of [Jakirlić and Hanjalić, 2002] in their figure (21) and with their model given in that paper by equations (5.1) and (5.2). A second point to notice is that the SPIV data, although partly affected by spatial filtering, give the same tendencies as the DNS. Another very remarkable point is the nearly perfect superposition of the channel and boundary layer DNS down to the wall, which means that the dissipation physics is very similar between the two

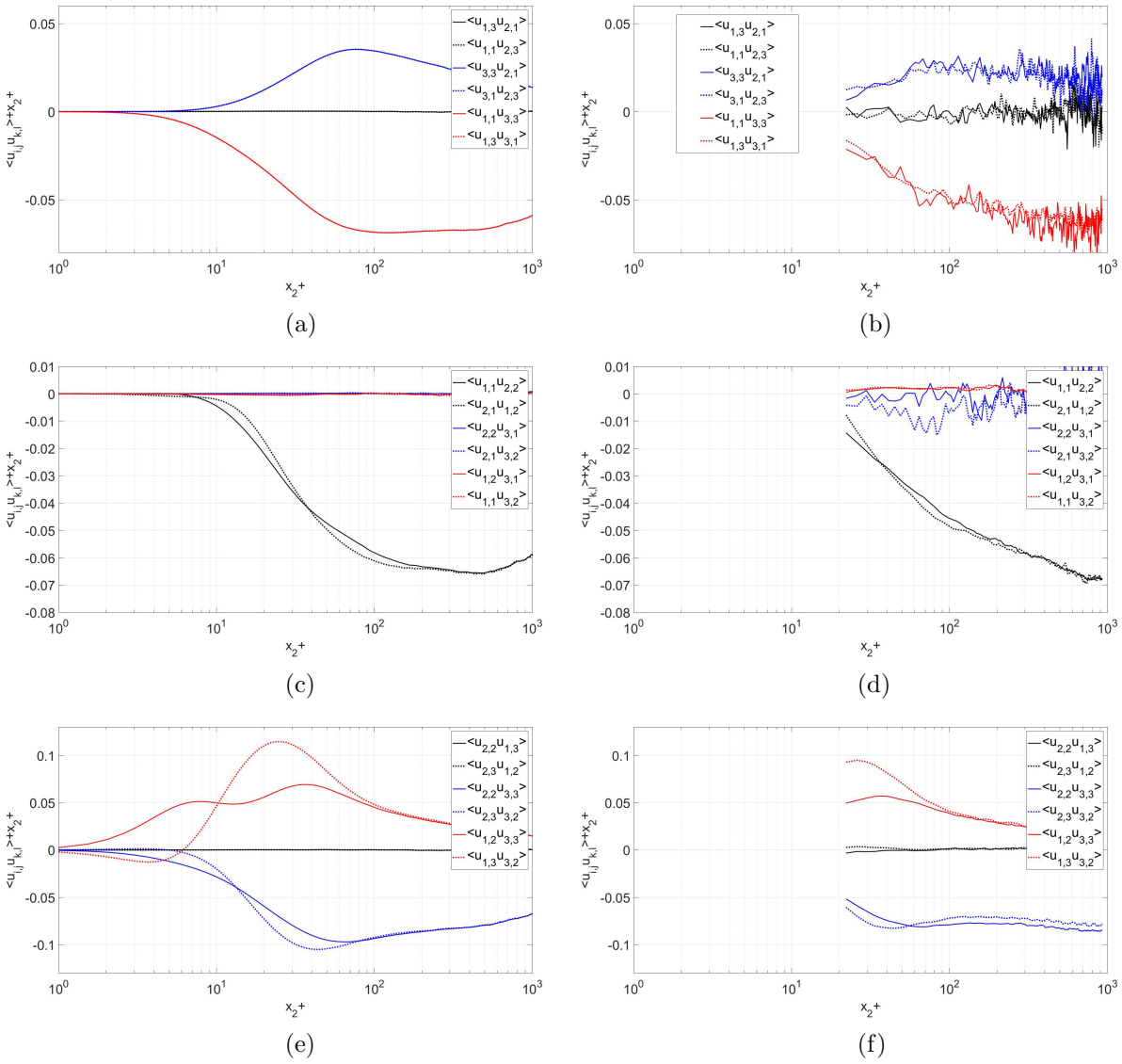

Figure 18: Homogeneity test for derivative moments from [Thais et al., 2011] DNS (left column) and SPIV (right column). Following equations (25), terms of the same color should superimpose. Note that ordinates have been multiplied by x_2^+. The correspondance with equation (25) is: (a) and (b) (1,2), (2,2), (3,2); (c) and (d) (1,1), (2,1), (3,1); (e) and (f) (1,3), (2,3), (3,3).

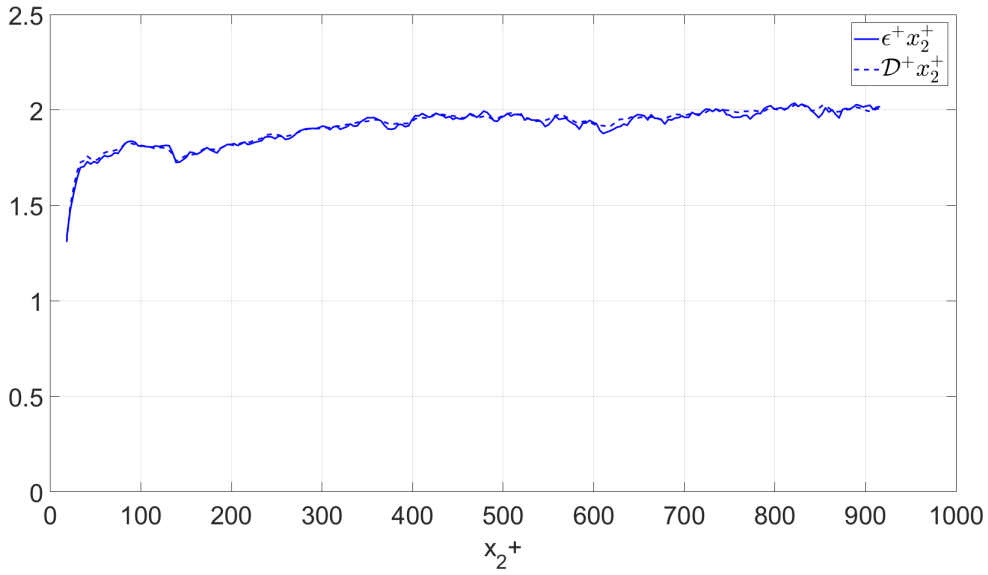

Figure 19: Comparison of premultiplied full ϵ and pseudo $\mathcal{D}$ dissipation in the overlap region from SPIV data in linear-linear representation.

flows[5]. Finally, one should point out the strong anisotropy between the three diagonal terms, with a clear domination of ϵ_{11} over the two others.

Now the key question is the behaviour of the pseudo-dissipation $\mathcal{D}_{ij}$ compared to the true dissipation tensor ϵ_{ij}. Figure 21 gives a lin-log plot of the three diagonal components of ϵ_{ij} (which, as shown above are the dominating ones) compared to the corresponding terms of $\mathcal{D}_{ij}$. The data are from the channel DNS. As can be seen, there is little difference between the corresponding components. This near equality was also noted by [Antonia et al., 1991] in their low Reynolds number channel DNS analysis. It is not obvious why this is true given our conclusions about the departures from *local homogeneity* based on figure 18.

9.2 Cross-derivative relations if the flow is only homogeneous in a plane.

Clearly none of the above analysis explains the near equality (if not exactly equality) of ϵ_{ij} and $\mathcal{D}_{ij}$ near the wall. One possibility that does not seem to have been previously considered is that this behavior might be a direct consequence of homogeneity only in the (x_1, x_3) plane. Certainly all experiments and DNS considered herein (and elsewhere) have one feature in common: they are homogeneous in the plane parallel to the wall. Note that this is exactly true for the channel, but approximately true for the boundary layers (and most free shear flows as well) due to their slow spreading rate.

What we would need to be true for $\mathcal{D}_{ij}$ and ϵ_{ij} to be equal is for the cross-derivative terms, $\langle \partial u_i/\partial x_j \, \partial u_j/\partial x_i \rangle$, to sum to zero without being able to use the fully-homogeneous condition of equation (23) to permute

[5]This is in spite of the fact that their Taylor expansions from the wall are different, namely the non-zero second-order term arising from the streamwise pressure gradient in the channel mean velocity.

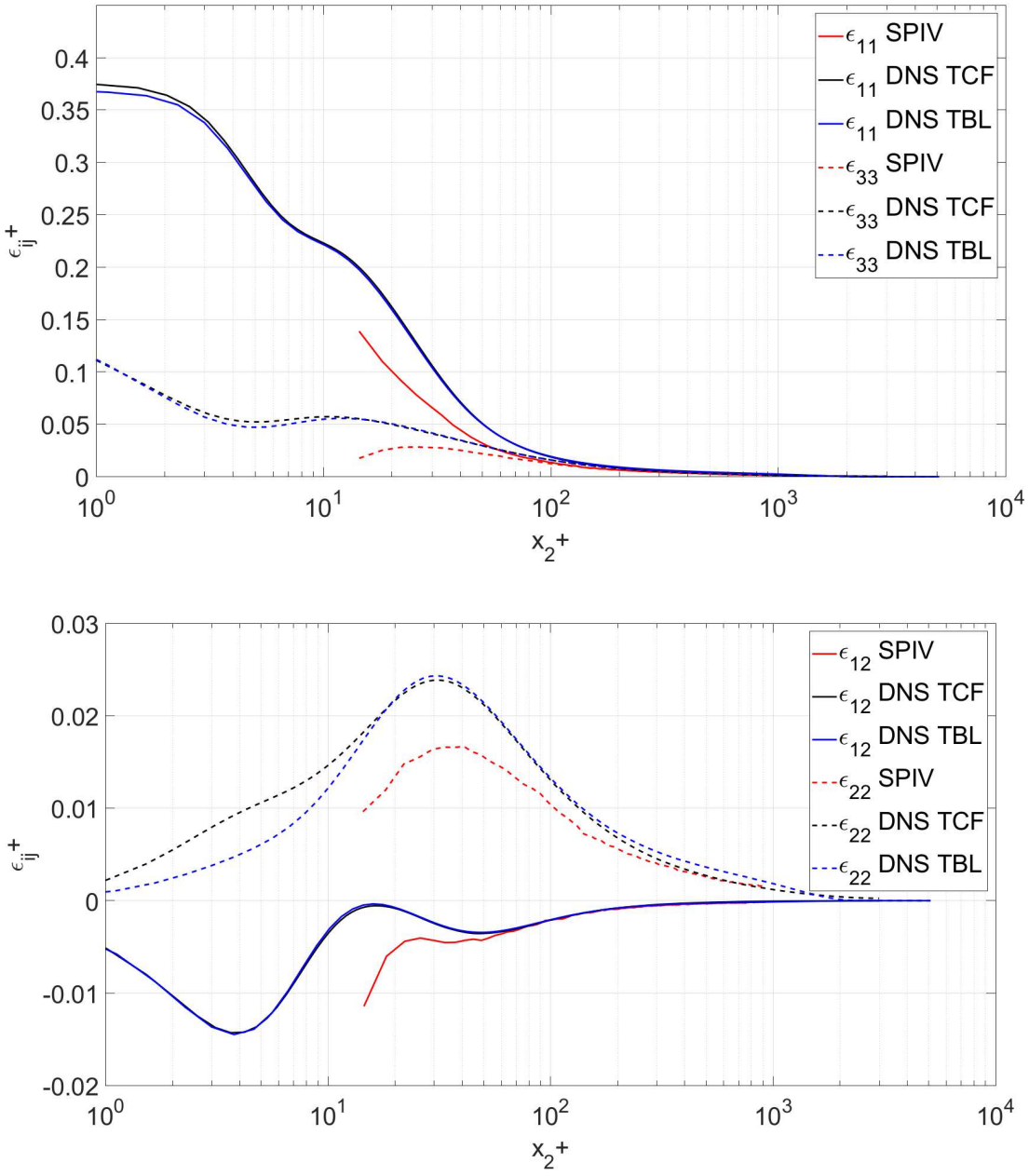

Figure 20: Diagonal terms, ϵ_{11}, ϵ_{22}, and ϵ_{33}, of the dissipation tensor, together with the shear stress component dissipation, ϵ_{12} from the SPIV boundary layer experiment (SPIV), the channel [Thais et al., 2011] DNS (TCF) and the boundary layer DNS of [Sillero et al., 2013] (TBL)

.

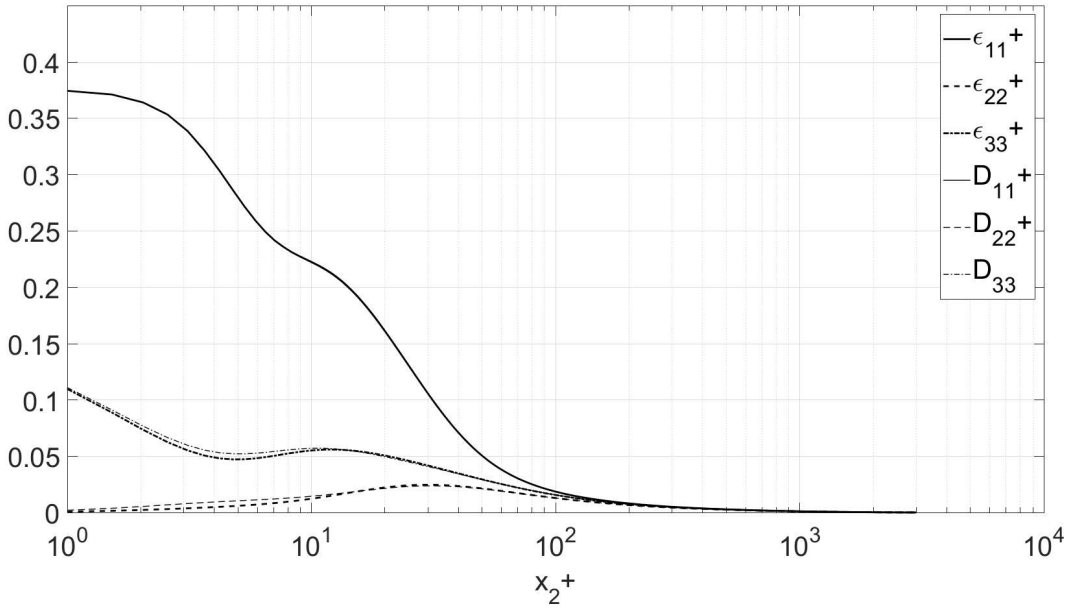

Figure 21: Comparison between the true dissipation tensor diagonal terms ϵ_{ii} and the pseudo dissipation ones $\mathcal{D}_{ii}$ using data from the [Thais et al., 2011] channel DNS.

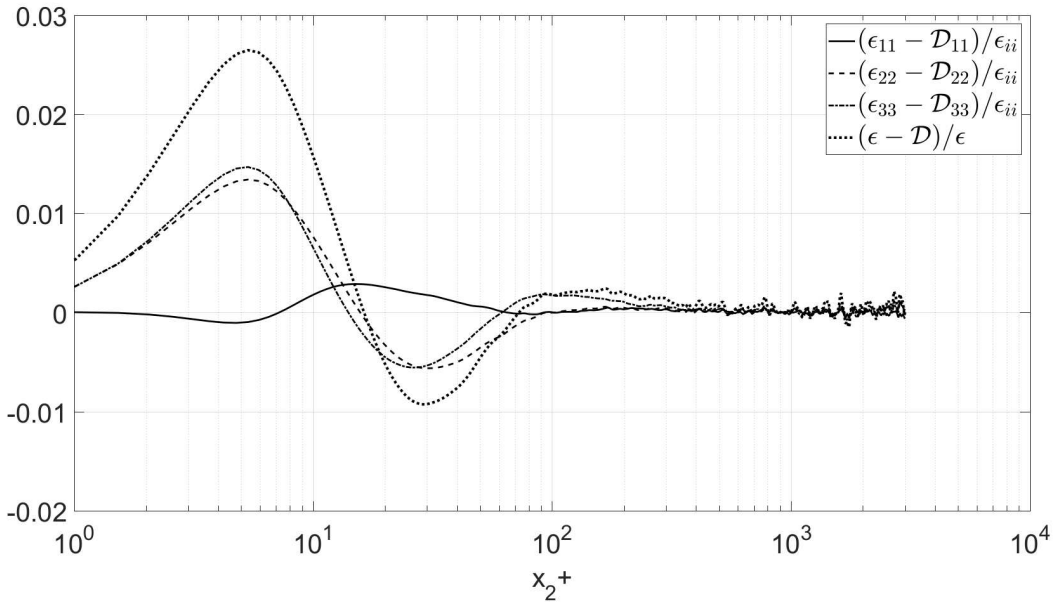

Figure 22: Difference between the normal components ϵ_{ii} and $\mathcal{D}_{ii}$ of the full and pseudo dissipation tensors and between ϵ and $\mathcal{D}$, data from the [Thais et al., 2011] channel DNS.

the indices. But this can be deduced from the continuity equation only if the following equalities hold:

$$\langle \frac{\partial u_1}{\partial x_1} \frac{\partial u_2}{\partial x_2} \rangle = \langle \frac{\partial u_1}{\partial x_2} \frac{\partial u_2}{\partial x_1} \rangle \tag{26}$$

$$\langle \frac{\partial u_1}{\partial x_1} \frac{\partial u_3}{\partial x_3} \rangle = \langle \frac{\partial u_1}{\partial x_3} \frac{\partial u_3}{\partial x_1} \rangle \tag{27}$$

$$\langle \frac{\partial u_2}{\partial x_2} \frac{\partial u_3}{\partial x_3} \rangle = \langle \frac{\partial u_2}{\partial x_3} \frac{\partial u_3}{\partial x_2} \rangle \tag{28}$$

In planar homogeneity parallel to the wall, equation (23) is restricted to permutation of m and n only equal to 1 and 3. The development of all the possibilities leads to the conclusion that only three equalities are meaningful and that only equation (27) is valid in plane homogeneous turbulence. This is confirmed by figure 18a which also shows that the two other equalites are exactly true in plane homogeneous turbulence, but neither of these appears in the dissipation. Figures 18e and 18f clearly show that the two other above equalities (26) and (28) are violated below $x_2^+ = 100$. So we have exactly what we need for only the 1-3 derivative moments. Unfortunately without assuming homogeneity in the 2-direction as well, it is impossible to derive a similar result for the other two mixed moments.

Figures 21 and 22 respectively plot the component dissipations and their differences. The clear and obvious conclusion is that $\mathcal{D}_{ij}$ and ϵ_{ij} (as well as $\mathcal{D}$ and ϵ) which must be fundamentally unequal, are in fact very close in practice down to the wall. Whether these slight differences are significant enough

for turbulence modellers to worry about is beyond the scope of this paper. But it surely provides an interesting question for theoreticians to ponder!

9.3 The dissipation anisotropy very near the wall

Figure 21 provides interesting information about the dissipation of the normal stresses. As can be seen, below $x_2^+ = 100$ this dissipation becomes very anisotropic, with $\mathcal{D}_{11}$ dominating the two other terms. A now classical way to examine the same data in terms of anisotropy is to look at the so-called 'Lumley-triangle' formed by plotting the second and third invariants of the dissipation anisotropy tensor (see [Chacin and Cantwell, 2000]). As in the region of interest ($x_2^+ < 100$) ϵ_{ij} and $\mathcal{D}_{ij}$ differ slightly, it is of interest to look at the anisotropy of both. The two invariants are obtained in the following manner for the full dissipation tensor ϵ_{ij}:

$$II_\epsilon = \epsilon_{ij}\epsilon_{ij}/2 \tag{29}$$

$$III_\epsilon = \epsilon_{ij}\epsilon_{jk}\epsilon_{ki}/3 \tag{30}$$

with similar relations for $II_\mathcal{D}$ and $III_\mathcal{D}$.

Figure 23 plots II versus III for both ϵ_{ij} and $\mathcal{D}_{ij}$ in the case of the channel DNS. Also shown are the usual limiting lines. Two inserts provide an enlarged view of two regions of interest. To the best of our knowledge this is the first time the diagrams for ϵ_{ij} and $\mathcal{D}_{ij}$ have been plotted together. [Antonia et al., 1991] did the same plot for ϵ_{ij} in the case of a channel flow at two Reynolds numbers of 3300 and 7900 (their figure 7b). The agreement with the present plot is very good, with most of the flow close to the axisymetric limit. A difference can be observed very near the wall where the turbulence is further from the one component limit (0.03,0.2) in the present data compared to (0.05, 0.25) for [Antonia et al., 1991]. Comparing ϵ_{ij} and $\mathcal{D}_{ij}$, one point of interest is that the curves begin to diverge only below $x_2^+ = 10$, and significantly around $x_2^+ = 5$. This is far below $x_2^+ = 100$ where local homogeneity was put in question.

Very similar results have been presented and discussed in detail for DNS channel flow for $\mathcal{D}_{ij}$ in the comprehensive papers by [Antonia et al., 1991] and [Gerolymos and Vallet, 2016] (Note that the latter incorrectly label $\mathcal{D}_{ij}$ the dissipation). [Antonia et al., 1991] also noticed that the preferred axis very close to the wall seemed to switch from the streamwise direction to normal to the wall, They apparently did not notice the failure of local homogeneity. Therefore we note that our results are virtually identical to the above contributions, and refer the reader to their papers. We do note three things, however. First the very near wall region ($x_2^+ < 5$) is nearly two-dimensional, not surprising given the suppression of the normal velocity component by the wall. Second, the diagram rapidly tends toward the axisymmetric asymptote, but never quite arrives. This is consistent with the idea of 'local' (but not complete) axisymmetry outside of $x_2^+ = 100$. And finally, we note that what might be interpreted as a trend toward isotropy appears to contradict the detailed analysis of Section 6 and of the above conclusions. Note that it is arguable whether there is a trend toward isotropy at all since all curves in figure 14 and 15 are maintaining the same relative distance from each other. Regardless, any tendency toward isotropy is well into the core region or outer boundary layer which was not considered in this paper.

9.4 Potential link to the near wall turbulence structure

It is of interest at this stage to try to understand better the physical origin of the anisotropy detailed above and the mechanisms at the origin of this dissipation. In the last 50 years, a large amount of research

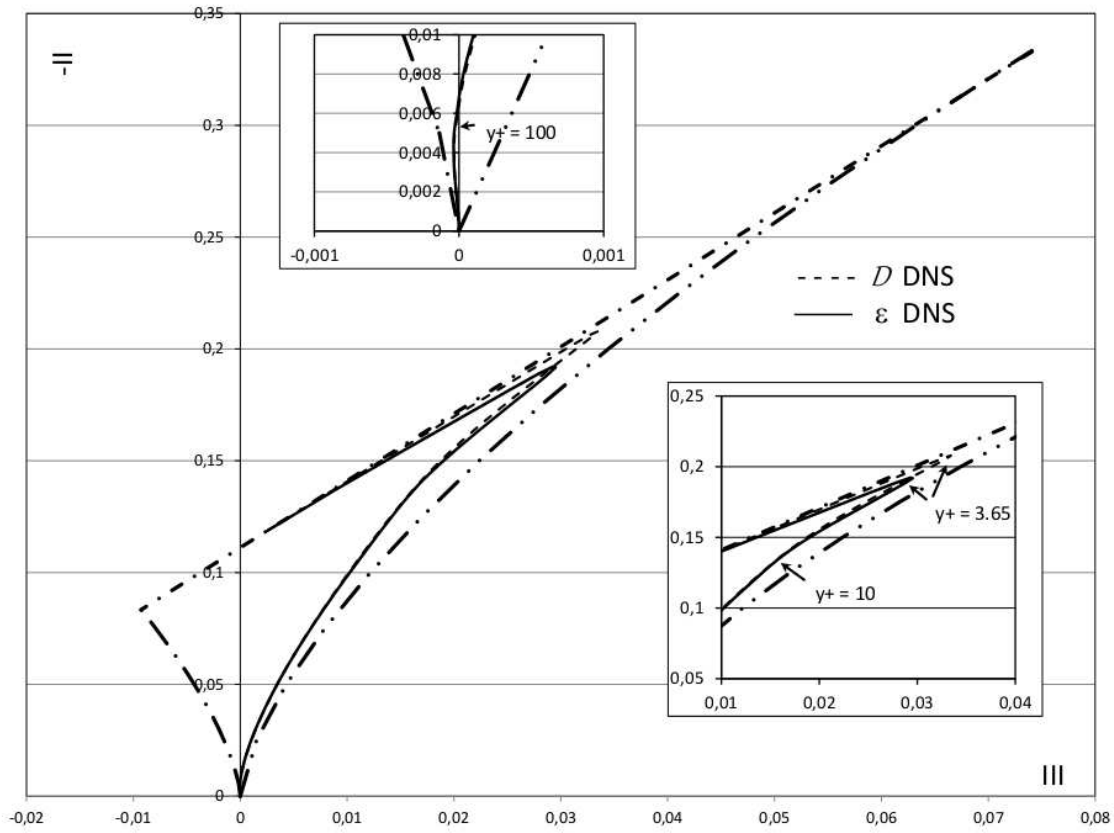

Figure 23: Lumley triangle for both ϵ_{ij} and $\mathcal{D}_{ij}$ computed from the present DNS data, with a zoom in the near wall region.

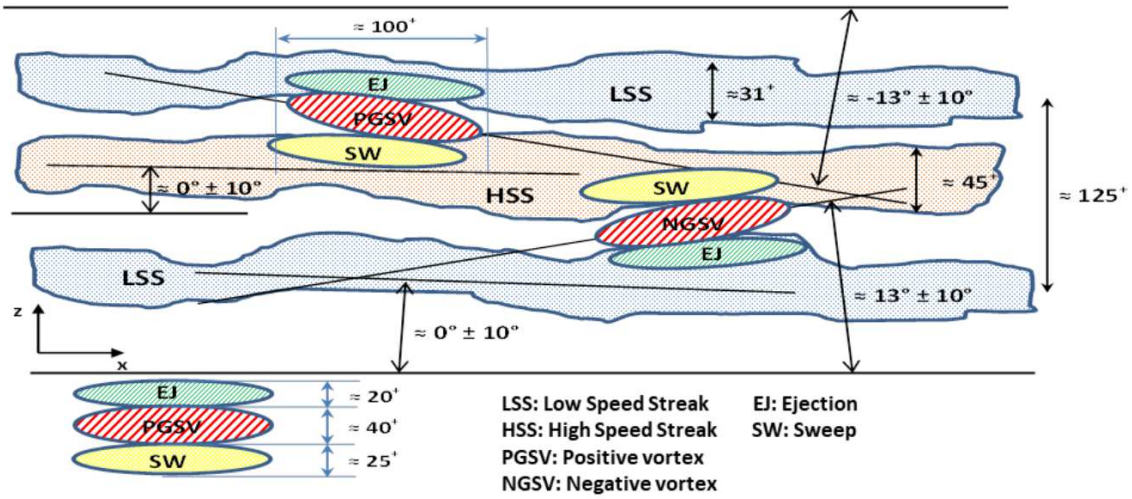

Figure 24: Sketch of the very near wall turbulence organization proposed by [Lin et al., 2008].

has been devoted to the study of the specific organization of turbulence near the wall (e.g.,[Theodorsen, 1952, Kline et al., 1967, Zhou et al., 1999, Panton, 1997]). Even if the outer part organisation is still a subject of intensive research with much to understand especially at high Reynolds number (see [Smits and Marusic, 2011]), the inner layer organization is fairly well characterized and understood (e.g.,[Jiménez and Pinelli, 1999, Kline and Portela, 1997]) A global picture including indications of scales is provided by [Lin et al., 2008] and reproduced in figure 24. The classical low and high speed streaks are sketched together with the quasi-streamwise vortices and sweeps and ejections. What is interesting is that the characteristic dimensions provided in this picture range from about $x_2^+ = 100$ to about $x_2^+ = 20$ (50 to 10 Kolmogorov units). It is clear from this sketch that this near wall organization is very far from the classical picture of homogeneous isotropic turbulence and of any cascade. The main difference is that production is now at scales which are the same as the dissipative scales.

It is interesting to note that although this 'turbulence organization' research has been very active around the world, it has stayed relatively disconnected from the modelling community and has not yet stimulated significant progress on the modelling side leading to a universal near wall model [6]. Having in-hand detailed information on a key unknown of turbulence, the dissipation tensor, and knowing now that most of its anisotropy is occuring in the region where the turbulence organization is reliably characterized, it is worth trying to see if this organization has any relation to the dissipation behaviour very near the wall. The pseudo-dissipation $\mathcal{D}_{ij}$ given by equation (6) can now be considered as the relevant tensor to represent dissipation and can be developed into the following for the diagonal terms and the main off-diagonal term $\mathcal{D}_{12}$:

[6]The WALLTURB European research project, which is at the origin of the present contribution, was aimed at that.

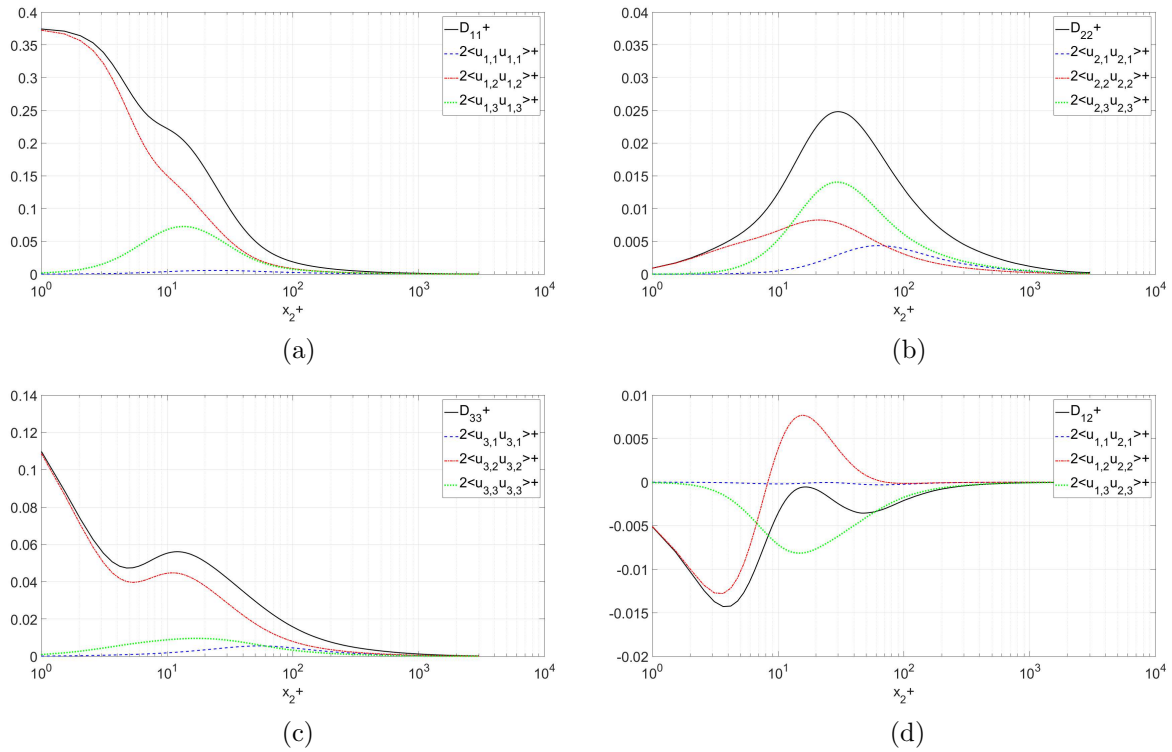

Figure 25: Derivative moments contributing to the main terms of the pseudo-dissipation tensor D_{ij}.

$$\mathcal{D}_{11} = 2\nu\langle\left[\frac{\partial u_1}{\partial x_1}\right]^2\rangle + 2\nu\langle\left[\frac{\partial u_1}{\partial x_2}\right]^2\rangle + 2\nu\langle\left[\frac{\partial u_1}{\partial x_3}\right]^2\rangle \quad (31)$$

$$\mathcal{D}_{22} = 2\nu\langle\left[\frac{\partial u_2}{\partial x_1}\right]^2\rangle + 2\nu\langle\left[\frac{\partial u_2}{\partial x_2}\right]^2\rangle + 2\nu\langle\left[\frac{\partial u_2}{\partial x_3}\right]^2\rangle \quad (32)$$

$$\mathcal{D}_{33} = 2\nu\langle\left[\frac{\partial u_3}{\partial x_1}\right]^2\rangle + 2\nu\langle\left[\frac{\partial u_3}{\partial x_2}\right]^2\rangle + 2\nu\langle\left[\frac{\partial u_3}{\partial x_3}\right]^2\rangle \quad (33)$$

$$\mathcal{D}_{12} = 2\nu\langle\frac{\partial u_1}{\partial x_1}\frac{\partial u_2}{\partial x_1}\rangle + 2\nu\langle\frac{\partial u_1}{\partial x_2}\frac{\partial u_2}{\partial x_2}\rangle + 2\nu\langle\frac{\partial u_1}{\partial x_3}\frac{\partial u_2}{\partial x_3}\rangle. \quad (34)$$

These show clearly the different velocity derivative moments contributing to each pseudo-dissipation component.

Figure 25 gives a plot of each of these moments for each of the pseudo-dissipation tensor terms of equations (31) to (34). For the first $\mathcal{D}_{11}$ term, the dominating contribution is clearly $\langle\left[\frac{\partial u_1}{\partial x_2}\right]^2\rangle$ which is maximum at the wall. The second pseudo-dissipation component $\mathcal{D}_{22}$ is an order of magnitude smaller

than the first one (as is the corresponding Reynolds stress). The peak of the two main contributing moments, $\langle\left[\frac{\partial u_2}{\partial x_2}\right]^2\rangle$ and $\langle\left[\frac{\partial u_2}{\partial x_3}\right]^2\rangle$, is located around the peak of TKE ($x_2^+ \simeq 15-20$), which is also the location of the center of the quasi-streamwise vortices as found by [Lin et al., 2008]. The last diagonal $\mathcal{D}_{33}$ term is, like the first one, largely dominated by one moment, $\langle\left[\frac{\partial u_3}{\partial x_2}\right]^2\rangle$, which is again maximum at the wall. Both $\mathcal{D}_{11}$ and $\mathcal{D}_{33}$ show a intriguing kink around $x_2^+ \simeq 15-20$. As could be expected, these three diagonal terms are mainly dominated by the moments corresponding to gradients normal to the wall which, consequently also dominate the scalar pseudo-dissipation $\mathcal{D}$.

In order to get a better insight into the structures contributing the most to these dissipative terms, figures 26 and 27 were built from the DNS of [Thais et al., 2011] in planes parallel to the wall at $x_2^+ = 3$ and $x_2^+ = 30$ respectively. The low (blue) and high (green) speed streaks are evidenced by thresholding the streamwise velocity fluctuations at the classical value of $\pm$ one rms (root mean square). The Q criterion, which is indicative of the presence of vortices, is given in red. The threshold was chosen to evidence the mostly vortical structures. The dominating moments of each of the diagonal terms of the $\mathcal{D}_{ij}$ tensor are also given in red. The threshold is twice the local mean value, that is the value on the curves of figure 25.

Looking first at figure 26 for $x_2^+ = 3$, it appears clearly from the Q criterion that the vortical activity is very limited. A striking similarity appears between this Q criterion and the term $[\partial u_2/\partial x_3]^2$ which is the dominant term of $\mathcal{D}_{22}$, indicating that this kind of dissipation is linked to strain rate which appears mostly on the side of the high speed streaks. The contrast is clear compared to $[\partial u_1/\partial x_1]^2$ and $[\partial u_2/\partial x_3]^2$ for which the red regions are much larger in scale and mostly located inside the high speed streaks.

Looking now at figure 27 for $x_2^+ = 30$, the first thing to notice from Q is that the number of vortical structures is much larger, that they are mostly streamwise oriented and elongated and that they effectively appear mostly between the streaks as sketched in figure 24. What is also clear from the moments is that all the dissipative activity is now strongly linked to these vortical structures and all at a comparable scale.

The conclusion which can be drawn from these two figures is that the dissipation very near the wall has two distinct physical origins. The first one, which dominates at the wall, is strongly linked to the high speed streaks, appears at spanwise scales comparable to them, and is probably related to the sweeping motions associated to these streaks. The second origin of dissipation is the vortical activity which is maximum around $x_2^+ = 20$ and which, looking back at figure 25, affects clearly all the components of $\mathcal{D}_{ij}$ at different levels and through different terms. It is interesting to notice at this stage that this wall location is also the place of a peak of production of TKE. [7]

In both of the cases evidenced in figures 26 and 27, we are very far from the classical Kolmogorov cascade and from the dissipation of TKE through the smallest eddies (The streamwise vortical structures are typically 10 Kolmogorov units in diameter and about 50 in length). Consequently, any attempt to model the near wall dissipation on the basis of the Kolmogorov theory has little chance to succeed. This probably explains the large number of near wall corrections available in the Reynolds Average Navier Stokes (RANS) literature.

[7] Part of the present results have been recently confirmed by the contribution of [Zaripov et al., 2020] who did study the extreme events of dissipation near the wall with the help of high-speed planar PIV. Their figure 7 is in fairly good agreement with what is observed in figure 26 here: the dissipation very near the wall, which is dominated by $[\partial u_1/\partial x_2]^2$ is mostly located at the bottom of the high speed streaks. As the technique used by these authors has access only to the information in the x_1, x_2 plane, they do not see the dissipation terms observed here further away from the wall at $x_2^+ = 30$ where they locate a high TKE production linked to the streamwise vortices.

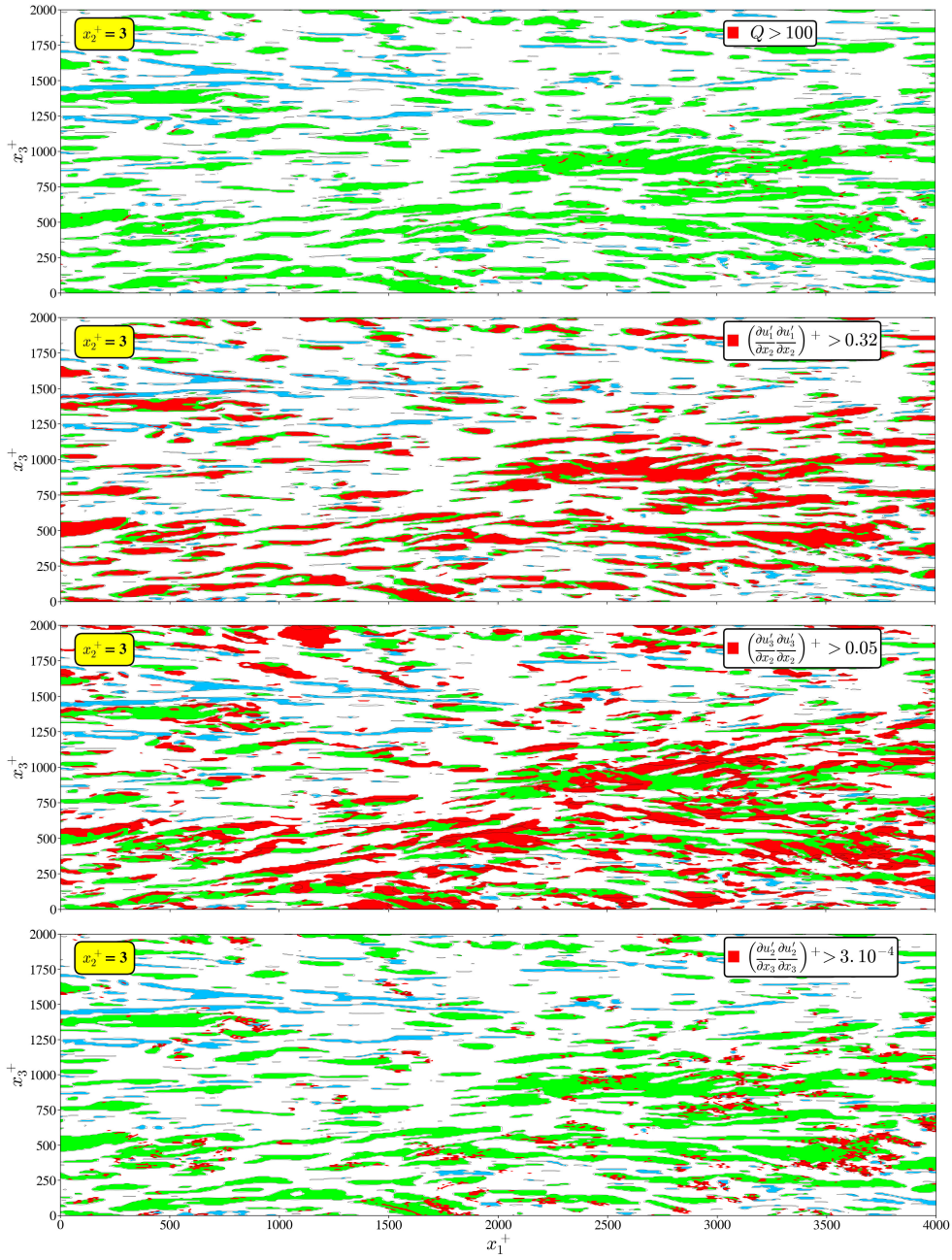

Figure 26: Instantaneous view of the derivative moments contributing to the main terms of the pseudo-dissipation tensor D_{ij} at $x_2^+ = 3$. High speed streaks: green, low speed streaks: blue. In red: (a) Q criterion, (b) main term of $\mathcal{D}_{11}$. (c) main term of $\mathcal{D}_{22}$. (d) main term of $\mathcal{D}_{33}$.

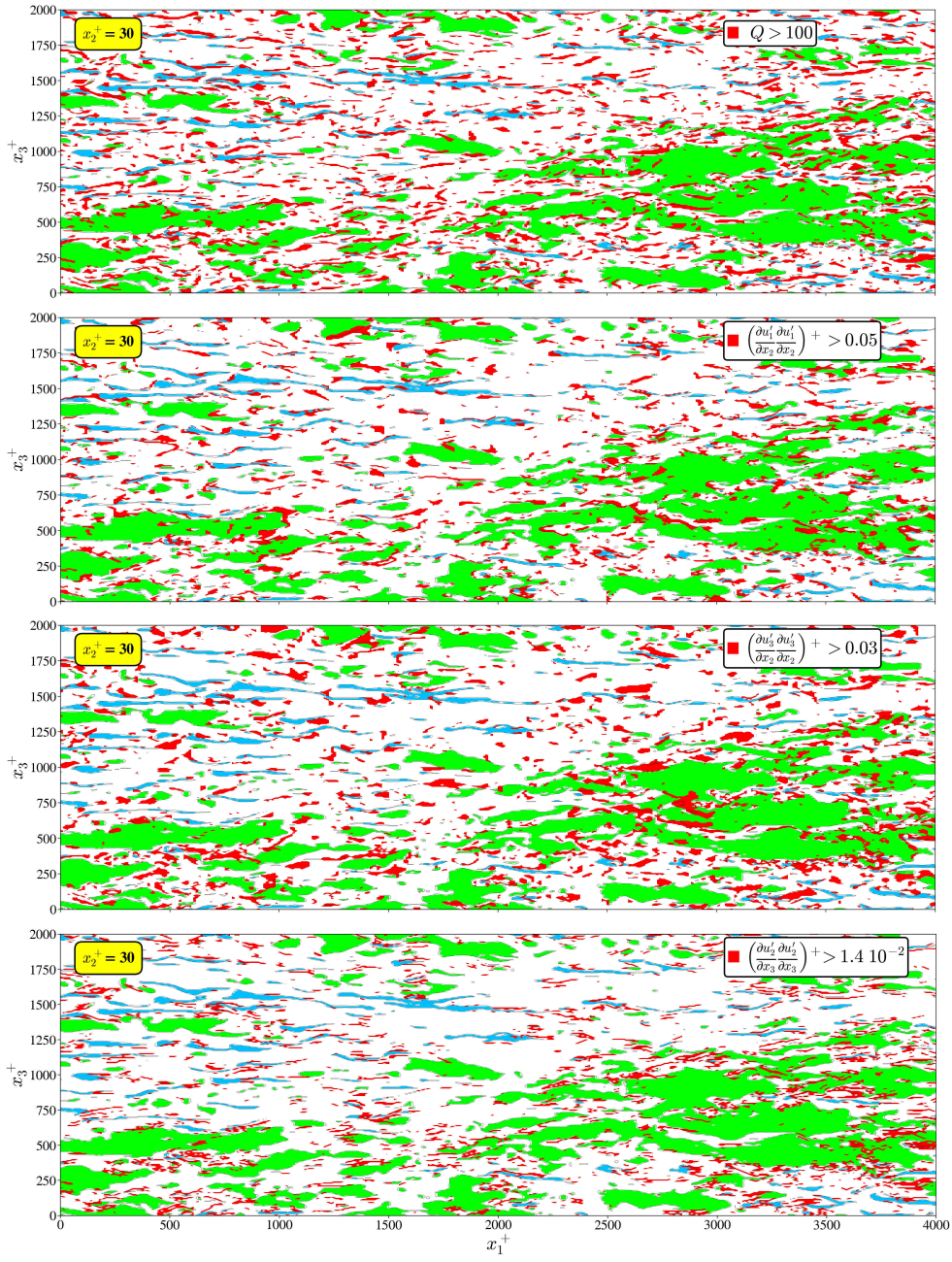

Figure 27: Instantaneous view of the derivative moments contributing to the main terms of the pseudo-dissipation tensor D_{ij} at $x_2^+ = 30$. High speed streaks: green, low speed streaks: blue. In red: (a) Q criterion, (b) main term of $\mathcal{D}_{11}$. (c) main term of $\mathcal{D}_{22}$. (d) main term of $\mathcal{D}_{33}$.

10 Summary and Conclusions

For both turbulence modeling and theoretical developments it is of prime importance to characterize the dissipation rate. This key parameter is difficult to access in practice as it involves all the terms of the strain-rate tensor and measurement requires a very good spatial resolution. With this objective, a specific SPIV experiment was carried out in the turbulent boundary layer which allowed derivative measurements of all three velocity components in all three space directions. Also, as a matter of validation and comparison, the data of a specific channel flow DNS at the same Reynolds number were processed to provide the same information.

This paper shows the measured dissipation in a boundary layer up to $x_2^+ \leq 1000$ ($x_2/\delta_{99} < 0.4$), and compares it to previous measurements and the channel flow DNS at similar Reynolds number. All of the experimental results show some evidence of spatial filtering, but taken together with the DNS give considerable insight into the dissipation.

For the first time, in the present experiment, all 12 terms contributing to the turbulence energy dissipation were measured directly using only spatial derivatives, and without any additional hypotheses. The results show that these terms behave quite differently in the inner part of the boundary layer. Despite an obvious spatial filtering, the hierarchy between the terms is in very good agreement with the DNS, except that the boundary layer data show generally a slightly better $1/x_2$ behaviour in the overlap region than the channel flow DNS. This could be attributed to the difference in flow type, but needs further investigation. Both the SPIV and the DNS data confirm that all the derivative cross-products are negative. Compared to the variances, they are about an order of magnitude smaller.

As far as the full dissipation is concerned, a thorough comparison with the data of [Honkan and Andreopoulos, 1997] showed that, after dividing their ϵ by 2 (in agreement with the authors) and removing the noise, they are in relatively good agreement with the present data and those of [Balint et al., 1991]. The three experiments were run at different Reynolds numbers (the present one being the highest) but at very comparable spatial resolutions when compared to the Kolmogorov scales. So, apart from the noise and the difference in measurement techniques, the differences between them can be attributed to the difference in Reynolds number or in the method used to assess the derivative moments. The difference in Reynolds number is too small to account for the differences. So it is most likely that the data processing is the most reliable explanation. As detailed in [Foucaut et al., 2021], a very careful procedure was used to denoise and validate the SPIV data. Finally, these SPIV data are very consistent with the DNS results.

Another important result of the present contribution is that the theoretical behavior ([George and Castillo, 1997, Wosnik et al., 2000]) of the dissipation in the inertial layer as $\epsilon^+ \approx \alpha {x_2^+}^{-1}$ (or weak power law behavior) is confirmed for the boundary layer with $\alpha \approx 2.0$. For the channel flow DNS, this is at least approximately true for $30 \leq x_2^+ \leq 600$, but a clear departure is observed in the outer region beyond $x_2/H = 0.2$, consistent with the very different physics in the outer flows. Also, it is observed that ϵ^+ and D^+ are nearly indistinguishable over the range of the measurements. This is quite surprising, since the hypothesis of local homogeneity near the wall breaks down inside $x_2^+ = 100$.

Having all the velocity derivative moments available from both experiment and DNS made it possible to check the classical hypotheses used to simplify turbulence theory. The results show that *local isotropy* is clearly a very bad assumption for this boundary layer flow within the overlap region and below. As evidenced by figures 14 and 15, several of the conditions set by equations (14-17) are violated by the derivative moments, and consequently, the estimation of the full dissipation on the basis of one single moment as done in equation (18) is quite risky. The streamwise mean square derivative, $\langle[\partial u_1/\partial x_1]^2\rangle$, is a particularly bad representative of the rest of the dissipation.

As far as *local axisymmetry* is concerned, it is observed that all conditions provided by equations (19) are fulfilled except two, as evidenced by figure 16. Nevertheless, in agreement with the observations of [Antonia et al., 1991, Zhao et al., 2015], *local axisymmetry* provides a very good approximation above $x_2^+ = 100$ and a reasonable one for $30 < x_2^+ < 100$, allowing us to propose simplified equations to evaluate the full TKE dissipation ϵ on the basis of only four derivative moments. These should be particularly useful to experimentalists using planar SPIV, since all the necessary terms can be measured in a plane.

The *local homogeneity* hypothesis appeared in fact to be the most interesting one as it implies directly that $\epsilon_{ij} = \mathcal{D}_{ij}$ and consequently that $\epsilon = \mathcal{D}$. As for local axisymmetry, the data show that *local homogeneity* is limited to the region above $x_2^+ = 100$ (Note that *local homogeneity* is a requisite for either *local axisymmetry* or *local isotropy* to be possible.). The data clearly show that *local homogeneity* is not valid below $x_2^+ = 100$.

In seemingly contradiction to the breakdown of local homogeneity, the full dissipation tensor can hardly be distinguished from the pseudo one below this wall distance. The analysis performed in section 9 shows that supposing homogeneity in planes parallel to the wall is enough to validate only one of the moments equalities demanded by equation (24) to have $\epsilon_{ij} = \mathcal{D}_{ij}$.

Looking at $\mathcal{D}_{ij}$, which on the basis of the present results can be considered as representative of the dissipation of the Reynolds stresses, it appears that the different moments building each component of this tensor do not have the same weight. The moments based on wall normal derivatives are mostly dominant, especially very near the wall. Looking at what is known of near wall turbulence organization and at some snapshots of the different terms in planes parallel to the wall, it appears that near wall dissipation is based on two different physical phenomenon. One dominating very near the wall is associated to the high speed streaks and to the sweeping motions embedded in them. The second one is clearly related to the quasi-streamwise vortices which have been observed by numerous authors around $x_2^+ = 20$ and which are at the origin also of the near wall turbulence production. Both phenomenon occur at fairly different scales. They appear in any case very different from the classical Kolmogorov cascade model. To go further, it would be of interest to extract from a sufficent number of independent realizations, length scales and intensity scales of the different dominant terms of $\mathcal{D}_{ij}$ evidenced here. This would most probably help a better modelling of the near wall dissipation which is critical to turbulence modelling (e.g. [Jakirlić and Hanjalić, 2002]).

From the authors point of view, the main contribution of the present work is to validate quantitatively, on the basis of both experimental and DNS high quality data the hypothesis made at the early stage of turbulence modelling to replace the full dissipation tensor in the Reynolds stress equation and the full dissipation in the turbulence kinetic energy equation by the corresponding pseudo-dissipation terms. This hypothesis was done at that time for the purpose of simplification (fewer terms to model) and because very little was known about dissipation. In about half a century, both direct simulation and experimental techniques have made enough progress to allow today a detailed analysis of the numerous dissipation components and an *a posteriori* validation of this well-known hypothesis. It should be noted however, that our theoretical conclusions are very much dependent on the assumptions that certain derivatives relations do not commute. If it can be argued that they do, then all of these conclusions near the wall will be purely a consequence of plane homogeneity. This will be especially problematical since ALL of the data is also homogeneous in planes. So fully three-dimensional flows could behave very differently.

Finally, the results obtained here clearly evidence that, except very near the wall ($x_2^+ < 100$), the *local homogeneity* hypothesis is remarkably good. So the *local axisymmetry* can be quite helpful as well to measure more accurately the scalar dissipation.

Acknowledgement

This work was supported through the International Campus on Safety and Inter modality in Transportation (CISIT). This work was carried out within the framework of the CNRS Research Federation on Ground Transports and Mobility, in articulation with the Elsat2020 project supported by the European Community, the French Ministry of Higher Education and Research, the Hauts de France Regional Council. Centrale Lille is acknowledged for providing regular financial support to the visits of Prof. William K. George and the "Région Nord Pas-de-Calais" for supporting his visit in 2009. This research has granted access to the HPC resources of [CCRT /CINES /IDRIS] under the allocation i20142b022277 and i20162a01741 made by GENCI (Grand Equipement National de Calcul Intensif). L. Thais is acknowledged for providing the data of his DNS of channel flow.

Declaration of interests. The authors report no conflict of interest.

Author contributions. C.C performed the PIV processing, J.M.F performed the PIV postprocessing and the corresponding figures. J.P.L performed the DNS postprocessing and the corresponding figures. W.K.G and M.S performed jointly the analysis and the writing of the paper.

Data availability statement. The data that support the findings of this study are openly available at https://turbase.cineca.it/init/routes/#/logging/view_dataset/66/tabmeta

Author ORCID. W.K. George https://orcid.org/ 0000-0002-3518-4431; M. Stanislas, https://orcid.org/0000-0001-6458-3936; J.M. Foucaut, https://orcid.org/0000-0003-0800-8608; C. Cuvier, https://orcid.org/0000-0001-6108-6942; J.P. Laval, https://orcid.org/0000-0003-2267-8376.

References

R.J. Adrian, C.D. Meinhart, and C.D. Tomkins. Vortex organization in the outer layer of the turbulent boundary layer. *J. Fluid Mech.*, 422:1–54, 2000.

Y. Andreopoulos and A. Honkan. An experimental study of the dissipative and vortical motions in a turbulent boundary layer. *J. Fluid Mech.*, 439:131–163, 2001.

R.A. Antonia, N. Phan-Thien, and A.J. Chambers. Taylor's hypothesis and the probability density of velocity and temporal derivatives in a turbulent flow. *J. Fluid Mech.*, 100:193 – 208, 1980.

R.A. Antonia, F. Anselmet, and A. J. Chambers. Assessment of local isotropy using measurements in a turbulent plane jet. *J. Fluid Mech.*, 163:365 – 391, 1986.

R.A. Antonia, J. Kim, and L.W.B. Browne. Some characteristics of small-scale turbulence in a turbulent duct flow . *J. Fluid Mech.*, 233:369–388, 1991.

J.L. Balint, J.M. Wallace, and P. Vukolavcevic. The velocity and vorticity vector-fields of a turbulent boundary-layer .2. statistical properties. *J. Fluid Mech.*, 228:53–86, 1991.

G. K. Batchelor, editor. *The theory of homogeneous turbulence*. Cambridge University Press, London, 1953.

G. K. Batchelor. The theory of axisymmetric turbulence. *Proc. R. Soc. Lond. A*, 186:480–502, 1954.

G.K.. Batchelor. *An Introduction to Fluid Dynamics*. CUP, Cambridge, UK, 1967.

J. Carlier and M. Stanislas. Experimental study of eddy structures in a turbulent boundary layer using particle image velocimetry. *J. Fluid Mech.*, 535:143–188, 2005.

J. M. Chacin and B. J. Cantwell. Dynamics of a low Reynolds number turbulent boundary layer. *J. Fluid Mech.*, 404:87–115, 2000.

F. H.. Champagne. The fine-scale structure of the turbulent velocity field. *J. Fluid Mech.*, 86:367–108, 1978.

S. Chandrasekar. The theory of axisymmetric turbulence. *Proc. R. Soc. Lond. A*, 242:557–577, 1950.

D Ewing and W. K.. George. The effect of cross flow on mean-square derivatives measured using hot wires. *Expts. in Fluids*, 29:418 – 428, 2000.

D Ewing, H. J. Hussein, and W. K.. George. Spatial resolution of parallel hot-wire probes for derivative measurements. *Experimental thermal and fluid science*, 11:155–173, 1995.

J. M. Foucaut and M. Stanislas. Some considerations on the accuracy and frequency response of some derivative filters applied to PIV vector fields. *Measurement Science and Technology*, 13:1058–1071, 2002.

J. M. Foucaut, W. George, M Stanislas, and C. Cuvier. Optimization of a SPIV experiment for derivative moments assessment in a turbulent boundary layert. *Experiments in Fluids*, 62(244), 2021. doi: https://doi.org/10.1007/s00348-021-03339-9.

J.-M. Foucaut, S. Coudert, M. Stanislas, and J. Delville. Full 3d correlation tensor computed from double field stereoscopic PIV in a high Reynolds number turbulent boundary layer. *Experiments in Fluids*, 50 (4, Sp. Iss. SI):839–846, APR 2011.

B. Ganapathisubramani, N. Hutchins, W. T. Hambleton, E. K. Longmire, and I. Marusic. Investigation of large-scale coherence in a turbulent boundary layer using two-point correlations. *Journal of Fluid Mechanics*, 524:57–80, 2005a.

B. Ganapathisubramani, E. K. Longmire, I. Marusic, and S. Pothos. Dual-plane PIV technique to determine the complete velocity gradient tensor in a turbulent boundary layer. *Experiments in Fluids*, 39:222–231, 2005b.

W. K. George. *Turbulence for the 21st Century*. on-line at http://www.turbulence-online.com, 2014.

W. K. George and L. Castillo. The zero pressure-gradient turbulent boundary layer. *Applied Mechanics Reviews*, 50:689–729, 1997.

W. K. George, H. J. Hussein, and S. H Woodward. An evaluation of the effect of a fluctuation convection velocity on the validity of Taylor's hypothesis. In *Proc. 10th Australasian Fluid Mech. Conf., Melbourne*, page 11.5, U. Melbourne, Melbourne, Australia, Dec. 1989.

W.K. George and H.J. Hussein. Locally axisymmetric turbulence. *J. Fluid Mech.*, 233:1–23, 1991.

W.K. George and D.B. Taulbee. Designing experiments to test closure hypothesis. *J. Exper. Thermal and Fluid Sci*, 3:249–260, 1992.

W.K. George and M. Tutkun. The mesolayer and Reynolds number dependencies of boundary layer turbulence. In Marusic I. Stanislas M., Jimenez J., editor, *Progress in Wall Turbulence: Understanding and Modeling. ERCOFTAC Series*, volume 14, pages 183–190. SPRINGER-VERLAG BERLIN, 2011.

G.A. Gerolymos and I. Vallet. The dissipation tensor ε_{ij} in wall turbulence. *J. Fluid Mech.*, 807:386–418, 2016.

G. Gulitski, M. Kholmyansky, W. Kinzelbach, B. Lthi, A. Tsinober, and S. Yorish. Velocity and temperature derivatives in high-Reynolds-number turbulent flows in the atmospheric surface layer. part 1. facilities, methods and some general results. *Journal of Fluid Mechanics*, 589:5781, 2007. doi: 10.1017/S0022112007007495.

W. T. Hambleton, N. Hutchins, and I. Marusic. Simultaneous orthogonal plane particle image velocimetry measurements in a turbulent boundary layer. *Journal of Fluid Mechanics*, 560:53–64, 2006.

S. Herpin, S. Coudert, J.-M. Foucaut, and M. Stanislas. Influence of the Reynolds number on the vortical structures in the logarithmic region of turbulent boundary layers. *Journal of Fluid Mechanics*, 716: 5–50, 2012.

A. Honkan and Y. Andreopoulos. Vorticity, strain-rate and dissipation characteristics in the near-wall region of turbulent boundary layers. *J. Fluid Mech.*, 350:29–96, 1997.

S. Hoyas and J. Jiménez. Scaling of the velocity fluctuations in turbulent channels up to $Re_\tau = 2003$. *Phys. Fluids.*, 18(011702), 2006.

S. Hoyas and J. Jiménez. Reynolds number effects on Reynolds-stress budgets in turbulent channels. *Phys. Fluids.*, 20(10):101511, 2008.

S. Jakirlić and K. Hanjalić. A new approach to modelling near-wall turbulence energy and stress dissipation. *Journal of Fluid Mechanics*, 459:139–166, 2002.

J. Jiménez and A. Pinelli. The autonomous cycle of near wall turbulence. *J. Fluid Mech.*, 389:335–359, 1999.

C. J. Kahler and M. Stanislas. Investigation of wall bounded flows by means of multiple plane stereo PIV. In *Proceedings of the 10th Int. Symp. on Appl. of Laser Tech. to Fluid Mech*, Lisbon, Portugal, 2000.

S. J. Kline and L. M. Portela. *A view of the structure of turbulent boundary layers.* Computational Mechanics Publications, R. Panton Editor, 1997.

S. J. Kline, W. C. Reynolds, F. A. Schraub, and P. W. Runstadler. The structure of turbulent boundary layers. *Journal of Fluid Mechanics*, 30:741–773, 1967.

A. N. Kolmogorov. The local structure of turbulence in incompressible viscous fluid for very large Reynolds numbers. *C. R. Acad. Sci. URSS*, 30:301–305, 1941.

M. Lee and R. D. Moser. Direct numerical simulation of turbulent channel flow up to $Re_\tau \simeq 5200$. *J. Fluid Mech.*, 774:395–415, 2015.

J. Lin, J.-P. Laval, J.-M. Foucaut, and M. Stanislas. Quantitative characterization of coherent structures in the buffer layer of near-wall turbulence. part 1: streaks. *Experiments in Fluids*, 45(6):999–1013, 2008.

J. L. Lumley. Interpretation of time spectra measured in high intensity shear flows. *Phys. Fluids*, 8:1056, 1995.

R. Manceau, J. R. Carlson, and T. B. Gatski. A rescaled elliptic relaxation approach: neutralizing the effect on the log layer. *Phys. Fluids*, 14(11):3868–3879, 2002.

R. (Ed.) Panton. Self-sustaining mechanisms of wall turbulence. *Computational Mechanics Publications, WIT Press.*, 1997.

M. Raffel, C. Willert, and J. Kompenhans. *Particle Image Velocimetry.* Springler-Verlag Berlin Heidelberg, 1998.

S. G. Saddoughi and S. V. Veeravalli. Local isotropy in turbulent boundary layers at high Reynolds number. *J. Fluid Mech.*, 268:333–372, 1994.

F Scarano. Iterative image deformation methods in PIV. *Measurement Science and Technology*, 13(1): R1–R19, 2002.

J.A. Sillero, J. Jimenez, and R.D. Moser. One-point statistics for turbulent wall-bounded flows at Reynolds numbers up to $\delta^+ \approx 2000$. *Phys. Fluids*, 25(105102), 2013.

A. J. Smits and I. Marusic. High Reynolds number Wall Turbulence. *Annu. Rev. Fluid Mech.*, 43: 353–375, 2011.

M. Stanislas, L. Perret, and J. M. Foucaut. Vortical structures in the turbulent boundary layer: a possible route to a universal representation. *J. Fluid Mech.*, 602:327–382, 2008.

G. I. Taylor. Statistical theory of turbulence. *Proc. R. Soc. London A*, 151:421 – 478, 1935.

H. Tennekes and J. L. Lumley. *A First Course in Turbulence.* MIT Press, Boston, 1972.

L. Thais, A. E. Tejada-Martínez, T. B. Gatski, and G. Mompean. A massively parallel hybrid scheme for direct numerical simulation of turbulent viscoelastic channel flow. *Comp. & Fluid*, 43:134–142, 2011.

T. Theodorsen. Mechanism of turbulence. In *Proc. ASME Midwest Conf. Fluid Mech.* 2^{nd} *Edn.*, pages 1–18, Columbus, OH, 1952.

A. Tsinober, E. Kit, and T. Dracos. Experimental investigation of the field of velocity gradients in turbulent flows. *J. Fluid Mech.*, 82:169–192, 1992.

M. Wänström, W.K. George, K. E. Meyer, and C. Westergaard. Identifying sources of stereoscopic PIV measurement errors on turbulent round jets. In *5th Joint ASME/JSME Fluids Engineering Conference*, San Diego, USA, 30 July -2 August, 2007 2007.

M. Wosnik, L. Castillo, and W.K. George. Theory for turbulent pipe and channel flows. *J. Fluid Mech.*, 421:115–145, 2000.

J. C. Wyngaard. Measurement of small-scale turbulence with hot wires. *J. Sci. Instruments*, 1:1105 – 1108, 1968.

D. Zaripov, R. Li, and N. Dushin. Dissipation rate estimation in the turbulent boundary layer using high-speed planar particle image velocimetry. *Exp. in Fluids*, 60-18, 2019. doi: 10.1007/s00348-018-2663-4.

D. Zaripov, R. Li, and I. Saushin. Extreme events of turbulent kinetic energy production and dissipation in turbulent channel flow: particle image velocimetry measurements. *Journal of Turbulence*, 21-1: 39–51, 2020. doi: 10.1080/14685248.2020.1727914.

F. Zhao, W.K. George, and B. G. M. van Wachem. Four-way coupled simulations of small particles in turbulent channel flow: The effects of particle shape and stokes number. *Physics of Fluids.*, 27(doi: http://dx.doi.org/10.1063/1.4927277):083301, 2015.

J. Zhou, R. J. Adrian, S. Balachander, and T. M. Kendall. Mechanisms for generating coherent packets of hairpin vortices in channel flow. *J. Fluid Mech.*, 387:353–396, 1999.